

HCN channels enhance spike phase coherence and regulate the phase of spikes and LFPs in the theta-frequency range

Manisha Sinha and Rishikesh Narayanan¹

Cellular Neurophysiology Laboratory, Molecular Biophysics Unit, Indian Institute of Science, Bangalore 560012, India

Edited by Terrence J. Sejnowski, Salk Institute for Biological Studies, La Jolla, CA, and approved March 24, 2015 (received for review October 2, 2014)

What are the implications for the existence of subthreshold ion channels, their localization profiles, and plasticity on local field potentials (LFPs)? Here, we assessed the role of hyperpolarization-activated cyclic-nucleotide-gated (HCN) channels in altering hippocampal theta-frequency LFPs and the associated spike phase. We presented spatiotemporally randomized, balanced theta-modulated excitatory and inhibitory inputs to somatically aligned, morphologically realistic pyramidal neuron models spread across a cylindrical neuropil. We computed LFPs from seven electrode sites and found that the insertion of an experimentally constrained HCN-conductance gradient into these neurons introduced a location-dependent lead in the LFP phase without significantly altering its amplitude. Further, neurons fired action potentials at a specific theta phase of the LFP, and the insertion of HCN channels introduced large lags in this spike phase and a striking enhancement in neuronal spike-phase coherence. Importantly, graded changes in either HCN conductance or its half-maximal activation voltage resulted in graded changes in LFP and spike phases. Our conclusions on the impact of HCN channels on LFPs and spike phase were invariant to changes in neuropil size, to morphological heterogeneity, to excitatory or inhibitory synaptic scaling, and to shifts in the onset phase of inhibitory inputs. Finally, we selectively abolished the inductive lead in the impedance phase introduced by HCN channels without altering neuronal excitability and found that this inductive phase lead contributed significantly to changes in LFP and spike phase. Our results uncover specific roles for HCN channels and their plasticity in phase-coding schemas and in the formation and dynamic reconfiguration of neuronal cell assemblies.

active dendrites | local field potential | neuronal inductor | phase coding | channel localization

Local field potentials (LFPs) have been largely believed to be a reflection of the synaptic drive that impinges on a neuron. In recent experimental and modeling studies, there has been a lot of debate on the source and spatial extent of LFPs (1–9). However, most of these studies have used neurons with passive dendrites in their models and/or have largely focused on the contribution of spike-generating conductances to LFPs (7, 8, 10, 11). Despite the widely acknowledged regulatory roles of subthreshold-activated ion channels and their somatodendritic gradients in the physiology and pathophysiology of synapses and neurons (12–17), the implications for their existence on LFPs and neuronal spike phase have surprisingly remained unexplored. This lacuna in LFP analysis is especially striking because local and widespread plasticity of these channels has been observed across several physiological and pathological conditions, translating to putative roles for these channels in neural coding, homeostasis, disease etiology and remedies, learning, and memory (16, 18–23).

In this study, we focus on the role of hyperpolarization-activated cyclic nucleotide-gated (HCN) channels that mediate the I_h current (I_h) in regulating LFPs and theta-frequency spike phase. From a single-neuron perspective, HCN channels in CA1 pyramidal neurons play a critical role in regulating neuronal integration and excitability (14, 24–27) and importantly introduce

an inductive phase lead in the voltage response to theta-frequency oscillatory inputs (28), thereby enabling intraneuronal synchrony of incoming theta-frequency inputs (29). Given these and their predominant dendritic expression (25), we hypothesized HCN channels as regulators of LFPs through their ability to alter the amplitude and phase of the intracellular voltage response, thereby altering several somatodendritic transmembrane currents that contribute to LFPs. The CA1 region of the hippocampus offers an ideal setup to test this hypothesis, given the regular, open-field organization (4, 6, 7) of the pyramidal neurons endowed with well-established somatodendritic gradients in ion channel densities (16). As this organization enables us to assess the role of location-dependent channel expression profiles on LFPs across different strata, we tested our hypothesis, using a computational scheme involving morphologically realistic, physiologically constrained conductance-based model neurons. Our results positively test our hypothesis and provide specific evidence for novel roles for HCN channels and their inductive component in regulating LFP and spike phases, apart from enhancing spike-phase coherence. These results identify definite roles for HCN channels in phase-coding schemas and in the formation and dynamic reconfiguration of neuronal cell assemblies and argue for the incorporation of subthreshold-activated ion channels, their gradients, and their plasticity into the computation of LFPs.

Results

We performed our experiments on a neuropil containing 440 morphologically realistic, conductance-based CA1 pyramidal neuronal models, whose somata were distributed within a cylindrical volume of 200 μm diameter and 40 μm height (Fig. 1A). We stimulated the neuronal compartments with theta-modulated

Significance

The impact of the pacemaking hyperpolarization-activated cyclic-nucleotide-gated (HCN) channels on local field potentials (LFP) has not been analyzed. Here, employing a neuropil of several morphologically precise hippocampal neuronal models that received systematically randomized rhythmic synaptic inputs, we demonstrate that HCN channels alter the phase, but not the amplitude, of LFPs. Further, it is known that the spike timings of individual neurons follow the beat of the LFPs and fire at precise phases of the LFP beat. We demonstrate that the presence of HCN channels alters this phase and enhances the precision to which the spikes follow the LFP beat. These results unveil several important roles for HCN channels, extending their regulatory potential beyond single-neuron physiology.

Author contributions: M.S. and R.N. designed research; M.S. performed research; M.S. analyzed data; and M.S. and R.N. wrote the paper.

The authors declare no conflict of interest.

This article is a PNAS Direct Submission.

¹To whom correspondence should be addressed. Email: rishi@mbu.iisc.ernet.in.

This article contains supporting information online at www.pnas.org/lookup/suppl/doi:10.1073/pnas.1419017112/-DCSupplemental.

high-conductance state (36), the LFP amplitudes across recording sites were not significantly different with the insertion of HCN channels. However, the incorporation of HCN channels introduced a significant location-dependent phase lead in the LFPs across all recording sites, when compared with corresponding LFPs computed in the absence of HCN channels (Fig. 2A). Assessing the mechanistic basis for this, we noted that the incorporation of HCN channels introduced an inductive lead in the intracellular local response voltage (28, 29) with reference to the response voltage in the passive neuron. Consequently, the transmembrane leak current in these compartments (which, by definition, followed the local voltage) exhibited a phase lead with reference to the leak current recorded in the absence of HCN channels. As LFPs are correlated with the net transmembrane

current, LFPs computed in the presence of HCN channels showed a phase lead across all strata in comparison to the LFPs computed in their absence (Fig. 2A). The phase of the local leak current and its somatodendritic distribution, in conjunction with the density of HCN channels (higher in distal apical dendrites) and the differential activation of HCN channels as a consequence of the relative phase difference and localization profiles of synaptic types (inhibition induces perisomatic hyperpolarization, whereas excitation induces SR depolarization, with a 60° phase shift) then explains the location dependence of LFP phase lead introduced by HCN channels. Consistent with this inference, we found that the LFP phase lead was graded and increased progressively with increase in HCN conductance (Fig. 2B), suggesting a graded influence of global HCN-channel plasticity on LFP phase.

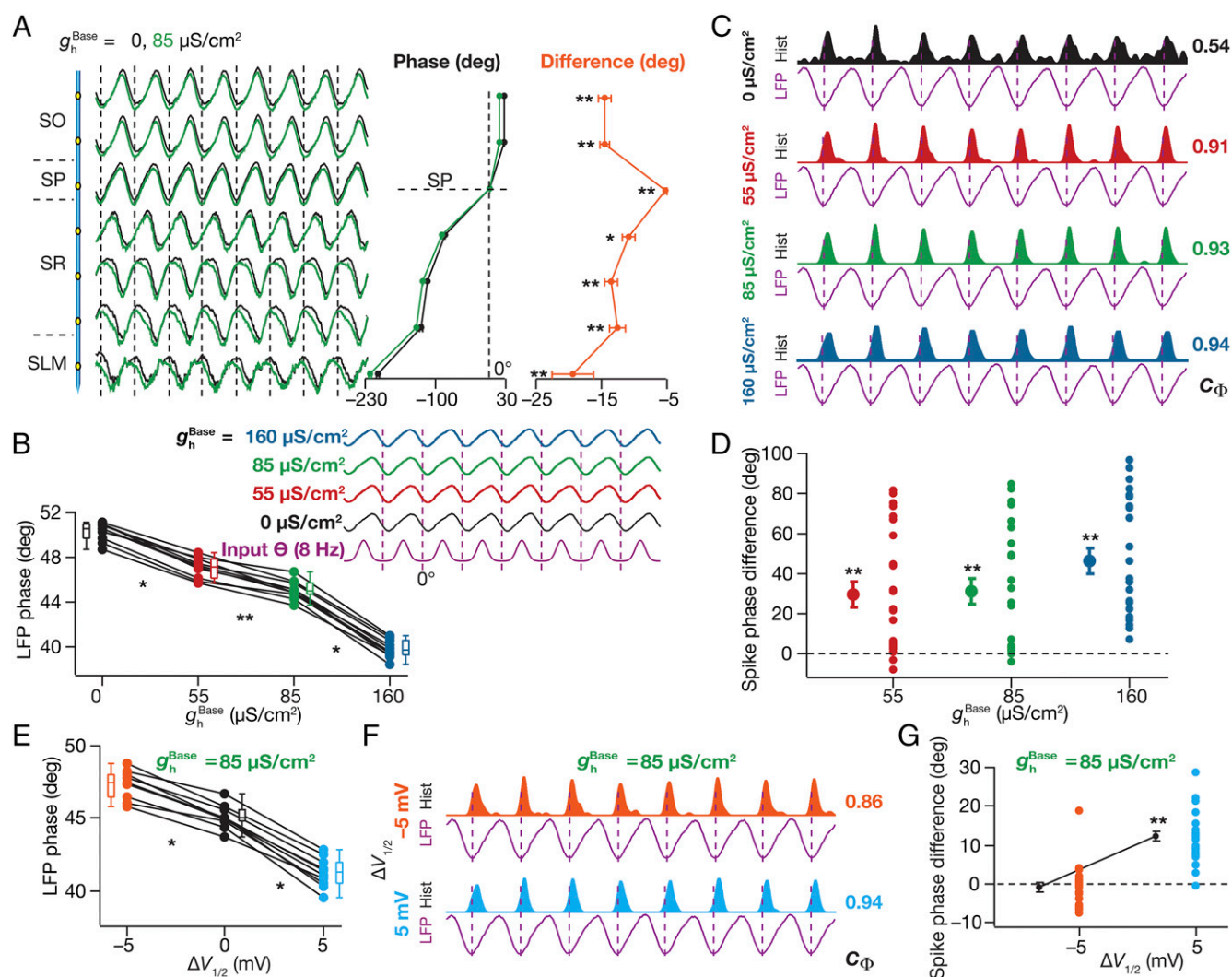


Fig. 2. Incorporating HCN channels resulted in a location-dependent lead in the LFP phase, a lag in the spike phase, and a reduction in spike-phase jitter. (A, Left) Normalized LFP traces (1 s) for different strata in the presence ($g_h^{\text{Base}} = 85 \mu\text{S}/\text{cm}^2$) and in the absence ($g_h^{\text{Base}} = 0 \mu\text{S}/\text{cm}^2$) of HCN channels. (A, Center) LFP phase (mean \pm SEM over 10 cycles) with reference to the stratum pyramidale (SP) LFP for corresponding traces in A, Left. (A, Right) Strata-wise cycle-matched difference (mean \pm SEM) between the LFP phase obtained with $g_h^{\text{Base}} = 85 \mu\text{S}/\text{cm}^2$ and $0 \mu\text{S}/\text{cm}^2$. (B, Top) Normalized LFP traces (1 s) for different g_h^{Base} values depicted with reference to the excitatory input θ . (B, Bottom) LFP phase (SP recording site) with reference to the excitatory input θ , plotted for different g_h^{Base} values. (C) Population spike time histograms (1 s) with corresponding SP LFP, plotted for different g_h^{Base} values. (D) Spike-phase difference (cycle matched for 8 cycles; mean \pm SEM) between the spike phase for the said g_h^{Base} value and for the case where $g_h^{\text{Base}} = 0 \mu\text{S}/\text{cm}^2$ ($n = 24$ neurons for $g_h^{\text{Base}} = 85 \mu\text{S}/\text{cm}^2$ and $160 \mu\text{S}/\text{cm}^2$). (E) LFP phase with reference to the excitatory input θ (mean \pm SEM, 10 cycles) for baseline $V_{1/2}$ ($\Delta V_{1/2} = 0$ mV) and hyperpolarized ($\Delta V_{1/2} = -5$ mV) and depolarized $V_{1/2}$ ($\Delta V_{1/2} = +5$ mV) of HCN-channel activation. (F) Population spike time histograms (1 s) with corresponding SP LFP with $\Delta V_{1/2} = -5$ mV and $\Delta V_{1/2} = +5$ mV. (G) Spike-phase difference (cycle matched for 8 cycles; mean \pm SEM) between the spike phase for the case where $\Delta V_{1/2} = -5/+5$ mV and those with $\Delta V_{1/2} = 0$ mV ($n = 24$ neurons). (A, B, and E) $*P < 0.05$, $**P < 0.005$ (Wilcoxon signed-rank test). (D and G) $**P < 0.005$ (Student's t test on the null hypothesis of no spike-phase difference).

HCN Channels Induced a Lag in the Spike Phase and Enhanced Neuronal Spike Phase Coherence. How does the presence of and plasticity in (26, 27) HCN-channel conductance alter the theta phase of neuronal spikes? We plotted the population spike-timing histogram and the corresponding SP LFP for each HCN-channel density under consideration (Fig. 2C). With increase in g_h^{Base} , we observed that the jitter associated with spike phases decreased, thereby enhancing their coherence with reference to the SP LFP (Fig. 2C). To quantify this, we calculated spike-phase coherence, C_Φ (37), and observed that C_Φ increased with increasing g_h^{Base} . This is consistent with earlier observations that HCN channels reduce temporal summation (14, 24–26), in effect reducing the temporal window for spike-generating coincidence detection (38, 39), a property that critically depends on their ability to introduce an inductive component (38). Specifically, the presence of HCN channels constricts the ability of a neuron to spike across a large span of the theta oscillation, thereby leading to enhanced spike-phase coherence (Fig. 2C). Finally, we found that the theta phase of the spikes showed a progressive and significant lag with increase in HCN-channel density (Fig. 2D), implying a graded influence of global HCN plasticity on spike phase.

Apart from changes in conductance, plasticity and cyclic nucleotide-dependent modulation of HCN channels have been demonstrated (40–43) to also manifest as shifts in their half-maximal activation voltage ($V_{1/2}$). To assess the impact of such shifts on LFP and spike phase, we repeated our simulations and analyses with different values of HCN-channel $V_{1/2}$ (Fig. 2E–G). We found that depolarization of $V_{1/2}$ resulted in an increased lead in LFP phase (Fig. 2E and Fig. S1D and E), an increased spike-phase coherence (Fig. 2F), and an increased lag in spike phase (Fig. 2G). We noted that our observations with depolarization of $V_{1/2}$ were similar to those with increase in g_h^{Base} (Fig. 2A–D). This should be expected given that I_h increases either with increase in g_h^{Base} or with depolarization of $V_{1/2}$, given similarities in the impact of either change on several intrinsic properties (26, 28).

Regulation of LFP and Spike Phases by HCN Channels Was Invariant to Changes in Neuropil Size and to Morphological Heterogeneity. Our analyses thus far were performed with a small 200- μm diameter cylindrical neuropil in an effort to reduce computational burden. How dependent were our conclusions on the size of the neuropil? To address this, we repeated our simulations with two additional neuropils with 400 μm diameter (total number of neurons: 1,797) and 1,000 μm diameter (total number of neurons: 11,297; Fig. 3A), while retaining the same density of neurons across neuropils and with identical electrode location at the center of the neuropil. As expected (7), the LFP amplitude increased with increase in neuropil size (Fig. 3B, Left and Fig. S2). However, the contribution per neuron from the distal annuli decreased by orders of magnitude (Fig. 3B, Right), suggesting minimal contribution of neurons from these annuli to the LFP. Importantly, the introduction of an HCN-channel gradient (Fig. 1C–E) into the constituent neurons resulted in a lead in the LFP phase without significant changes in LFP amplitude (Fig. 3B–D and Fig. S2), an increase in spike-phase coherence (Fig. 3E), and a lag in the associated spike phase (Fig. 3F) across all tested neuropils.

Next, although our analyses thus far were performed with independently rotated versions of a morphological reconstruction with randomly located probabilistic synaptic input (7), they were derived from a single morphological reconstruction (*n123*; Fig. 1A). To address the impact of morphological heterogeneity, we employed an additional morphological reconstruction (*ri04*; Fig. S3A), tuned its intrinsic and synaptic properties along its somatodendritic arbor to match with experimental observations (Fig. S3B–E), and uniformly distributed the two morphologies with random rotations across the neuropil (Fig. 3G). Comparing LFPs

and spikes obtained in the absence and the presence of HCN channels, we found the impact of HCN channels in introducing a lead in LFP phase (Fig. 3H and Fig. S3F and G), an increase in spike-phase coherence (Fig. 3I and Fig. S3H), and a lag in spike phase (Fig. 3J) to be invariant to morphological heterogeneity. Together, these results suggested that the impact of HCN channels on LFP phase, spike phase, and spike coherence was invariant to changes in neuropil size and to morphological heterogeneity.

Regulation of LFP and Spike Phases by HCN Channels Was Invariant to Changes in Synaptic Parameters. Were our conclusions on the role of HCN channels in altering LFP and spike phases (Figs. 2 and 3) specific to our choice of parameters associated with the excitatory and inhibitory drive? To address these, we performed detailed sensitivity analyses on parameters (Fig. 4 and Figs. S4–S7) associated with excitatory and inhibitory synapses. We found that the introduction of HCN channels resulted in a lead in the LFP phase, an enhancement in spike-phase coherence, and a lag in the spike phase, irrespective of up- or down-regulation of excitatory (Fig. 4A–C) or inhibitory (Fig. 4D–F) synapses. Next, we reanalyzed the data presented in Fig. 4A–F to ask whether synaptic scaling of excitatory or inhibitory inputs altered LFPs and spikes. Whereas increasing AMPAR conductances induced a lag in the SP LFP and a lead in the spike phase (Fig. S4), increase in GABA_A conductances resulted in a lead in the SP LFP and a lag in the spike phase (Fig. S5). We noted that the spike-phase coherence was not significantly altered by synaptic scaling (Fig. 4B and E and Figs. S4 and S5).

How dependent were our conclusions on the specific choice of the phase difference, ϕ_{gin} , between the excitatory and inhibitory theta-frequency synaptic inputs, thus far fixed at 60°? We changed ϕ_{gin} to various values and compared LFPs and spike phases across different values of ϕ_{gin} in neurons, in the presence or the absence of HCN channels. We found that the introduction of HCN channels resulted in a lead in the LFP phase, an enhancement in spike-phase coherence, and a lag in the spike phase, irrespective of the specific value of ϕ_{gin} (Fig. 4G–I). Next, we reanalyzed the data presented in Fig. 4G–I to ask whether changes in ϕ_{gin} altered LFPs and spikes. We observed a striking shift in the SP LFP phase on changing ϕ_{gin} , with the LFP phase leading by $\sim 120^\circ$ when ϕ_{gin} shifted from -60° to 60° , a magnitude of shift that strictly followed magnitude of change in ϕ_{gin} (Fig. 4G and Fig. S6). Although we did not observe any significant difference in the population spike-phase coherence on changing ϕ_{gin} (Fig. 4H and Fig. S6), spike phase displayed a dependence that would be expected from the shift in SP LFP. Specifically, shifting ϕ_{gin} from -60° to 60° resulted in $\sim 120^\circ$ lag in the spike phase (Fig. S6). Finally, we performed a sensitivity analysis on the reversal potential of the GABA_A receptor and found that except for the expected change in LFP amplitude due to changes in driving force, our conclusions on the impact of HCN channels were invariant to changes in the reversal potential of the GABA_A receptor (Fig. S7).

Together these results suggest that our conclusions on HCN-channel regulation of LFPs and spikes were invariant to changes in synaptic parameters. Further, these results also reveal an important role for synaptic scaling and for temporal structure of excitatory–inhibitory inputs in regulating LFP and spike phases, but not in spike-phase coherence.

A Single Neuron Can Shift Its Spike Phase Through HCN Plasticity. The kind of global changes in HCN channel density spanning a large set of neurons that we assessed thus far have been shown to occur only under pathophysiological conditions (18–20, 22, 23). Under physiological conditions, neurons are known to shift their spike phase over a course of time, either as part of a behavioral task or in the process of the neuron being reassigned to another cell assembly (33–35). As HCN plasticity has been demonstrated

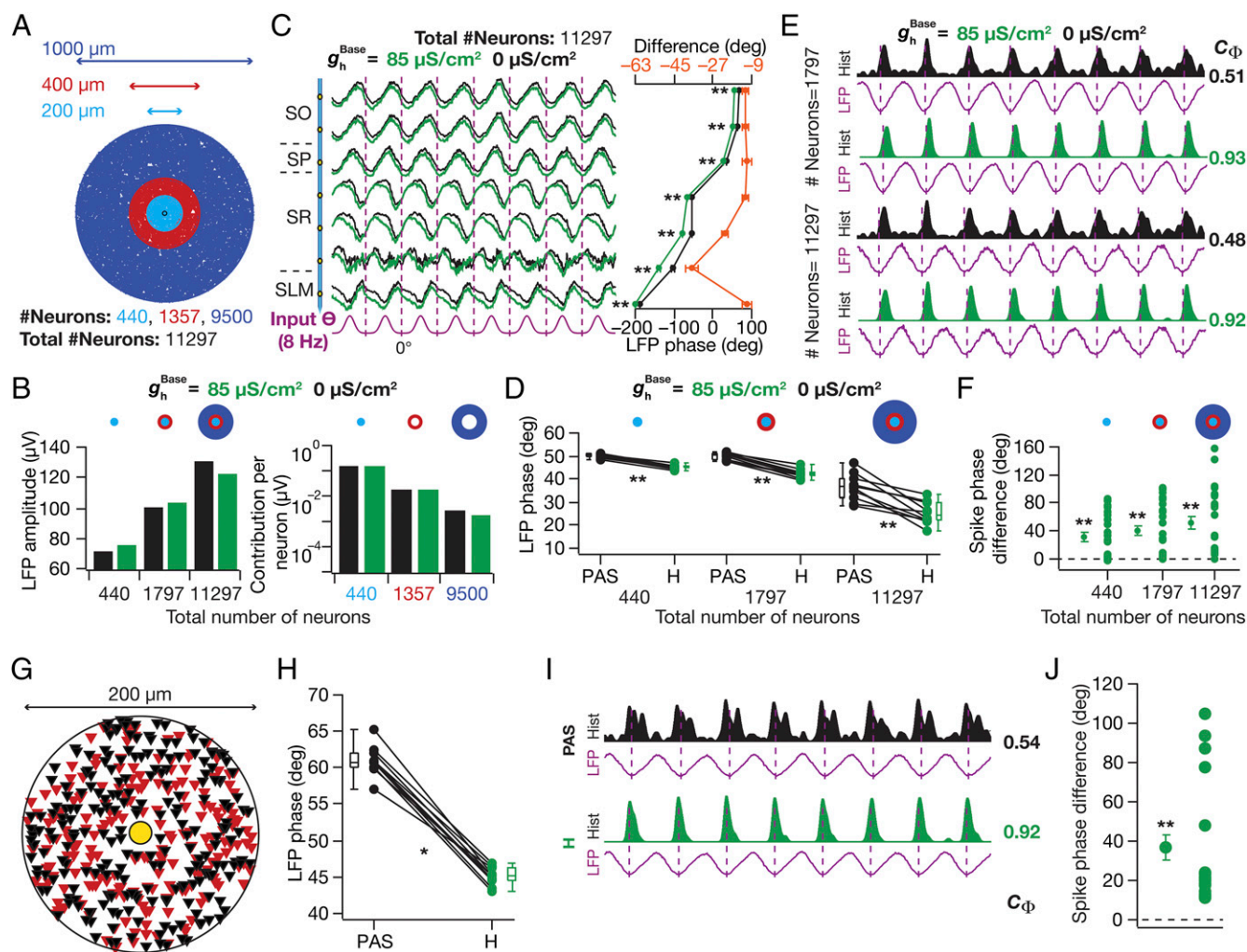


Fig. 3. HCN-channel-induced changes in LFP and spike phases were invariant to changes in neuropil size and to morphological heterogeneity. (A) Three neuropils of different sizes, used for analyses presented in B–F, depicted with the distribution of neurons. (B, Left) SP LFP amplitude computed in the presence ($g_h^{\text{Base}} = 85 \mu\text{S}/\text{cm}^2$) and in the absence ($g_h^{\text{Base}} = 0 \mu\text{S}/\text{cm}^2$) of HCN channels, for three different neuropil sizes. (B, Right) Per neuron contribution to the LFP amplitude computed with $g_h^{\text{Base}} = 0 \mu\text{S}/\text{cm}^2$ and $85 \mu\text{S}/\text{cm}^2$ for the three annuli (A). (C, Left) Normalized LFP traces (1 s) for different strata with $g_h^{\text{Base}} = 0 \mu\text{S}/\text{cm}^2$ and $85 \mu\text{S}/\text{cm}^2$ for the largest (1,000 μm diameter) neuropil. (C, Right, Bottom axis) LFP phase with reference to the excitatory input θ (mean \pm SEM, 10 cycles) for corresponding traces in C, Left. (C, Right, Top axis) Strata-matched phase difference between LFPs obtained with $g_h^{\text{Base}} = 85 \mu\text{S}/\text{cm}^2$ and $0 \mu\text{S}/\text{cm}^2$. (D) LFP phase with reference to the excitatory input θ for three different neuropil sizes computed in the absence (PAS) and the presence (H) of HCN channels. Note the increased variability in the LFP phases (computed across cycles) with increase in neuropil size, a consequence of increased jitter in LFP traces with increase in neuropil size (Fig. S2). (E) Population spike-time histograms (1 s) with corresponding SP LFP for different neuropil sizes for $g_h^{\text{Base}} = 0 \mu\text{S}/\text{cm}^2$ and $85 \mu\text{S}/\text{cm}^2$. (F) For three neuropil sizes, cycle-matched difference between spike phases obtained with $g_h^{\text{Base}} = 85 \mu\text{S}/\text{cm}^2$ and with $g_h^{\text{Base}} = 0 \mu\text{S}/\text{cm}^2$, for 24 different neurons (mean \pm SEM). (G) Distribution of 440 neurons with *n123* (red, $N_n = 214$) and *ri04* (black, $N_n = 226$) morphological reconstruction, used for the analyses in H–J. (H) SP LFP phase with reference to input θ (mean \pm SEM, 10 cycles), computed in the absence (PAS) and the presence (H) of HCN channels. (I) Population spike-time histograms (1 s) with corresponding SP LFP. (J) Cycle-matched difference between spike phases obtained in the presence and in the absence of HCN channels, for 22 different neurons (mean \pm SEM). (C, D, and H) $*P < 0.05$, $**P < 0.005$ (Wilcoxon signed rank test). (F and J) $**P < 0.005$ (Student's *t* test on the null hypothesis of no spike-phase difference).

to accompany bidirectional synaptic plasticity (16, 22, 24, 26–28) and plasticity in one or few neurons is physiologically more plausible, we asked whether plasticity in HCN channel density of a single neuron was sufficient to alter its spike phase.

We altered the g_h^{Base} of a single neuron whose soma was located among those closest to the electrode to three different values (as in Fig. 2 B–D), while g_h^{Base} of all other neurons was set at $85 \mu\text{S}/\text{cm}^2$ (Fig. 5A). Despite such proximal positioning, we observed no significant difference in the LFP amplitude (Fig. 5B) or phase (Fig. 5C) with plasticity in HCN channels of the neuron. This was to be expected because the LFP was calculated using compartments from 440 neurons, and a change in HCN-channel density in one neuron should not alter the LFP signifi-

cantly. Next, we computed the spike phase of the chosen neuron with reference to the corresponding LFPs and compared them across different values of its g_h^{Base} (Fig. 5D). We found no significant difference in the spike phase of the neuron when g_h^{Base} was decreased, but observed a significant lag in the spike phase with higher g_h^{Base} . We repeated the procedure across all input structures that elicited spikes (24 of 25), by replacing the neuron at the specified location (Fig. 5A) by each of the remaining 23 spiking neurons, and found our conclusions to be robust across different input structures (Fig. 5D). These results suggested that HCN-channel plasticity could act as a putative mechanism for a neuron to shift its spike phase with reference to an externally driven theta oscillation (4, 33, 35, 44).

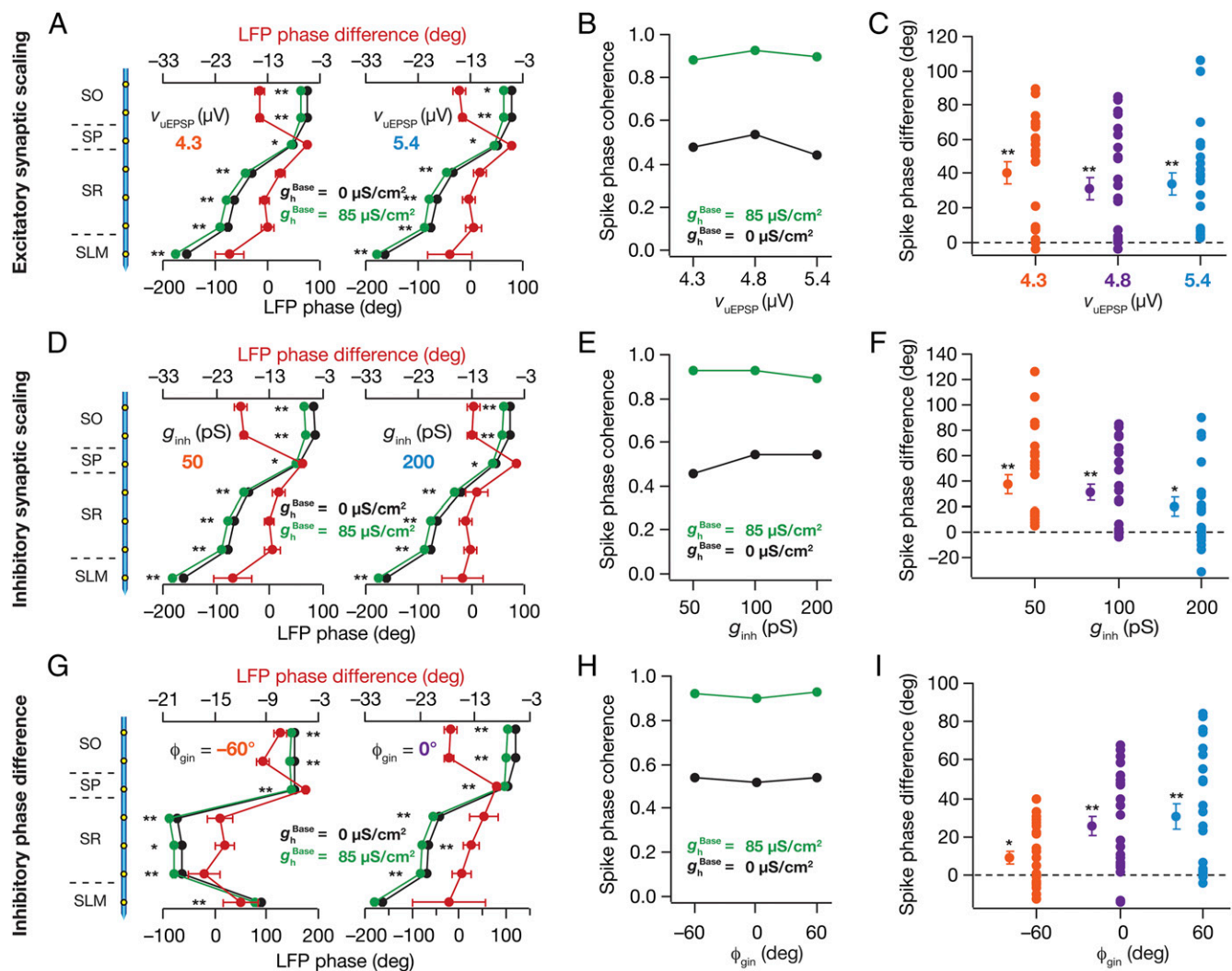


Fig. 4. HCN-channel-induced changes in LFP and spike phases were invariant to changes in synaptic properties. (A, Bottom axis) LFP phase with reference to the excitatory input θ (mean \pm SEM, 10 cycles), computed in the presence ($g_h^{\text{Base}} = 85 \mu\text{S}/\text{cm}^2$) and in the absence ($g_h^{\text{Base}} = 0 \mu\text{S}/\text{cm}^2$) of HCN channels for different unitary EPSP (v_{UEPSP}) values. Default value of $v_{\text{UEPSP}} = 4.8 \mu\text{V}$. (A, Top axis) Strata-matched phase difference between LFPs obtained with $g_h^{\text{Base}} = 85 \mu\text{S}/\text{cm}^2$ and $0 \mu\text{S}/\text{cm}^2$. (B) Spike-phase coherence plotted for different v_{UEPSP} values, for $g_h^{\text{Base}} = 0, 85 \mu\text{S}/\text{cm}^2$. (C) Cycle-matched difference between spike phases obtained with $g_h^{\text{Base}} = 85 \mu\text{S}/\text{cm}^2$ and with $g_h^{\text{Base}} = 0 \mu\text{S}/\text{cm}^2$ for different neurons (mean \pm SEM), plotted for each v_{UEPSP} . (D–F) Same as A–C, but for different values of inhibitory synaptic conductance (g_{inh}). Default value of $g_{\text{inh}} = 100 \text{ pS}$. (G–I) Same as A–C, but for different values of phase difference (ϕ_{gin}) between the excitatory and inhibitory theta-frequency synaptic inputs. Default value of $\phi_{\text{gin}} = 60^\circ$. Spike phases: $n = 22$ neurons for $v_{\text{UEPSP}} = 4.3 \mu\text{V}$, $n = 23$ neurons for $g_{\text{inh}} = 200 \text{ pS}$, $n = 24$ neurons for $v_{\text{UEPSP}} = 4.8 \mu\text{V}$, for $g_{\text{inh}} = 100 \text{ pS}$ and for $\phi_{\text{gin}} = 0^\circ$ and 60° . (A, D, and G) $*P < 0.05$, $**P < 0.005$ (Wilcoxon signed-rank test). (C, F, and I) $**P < 0.005$ (Student's t test on the null hypothesis of no spike-phase difference).

A Faster HCN Channel Nullified Inductive Impedance Without Altering Intrinsic Excitability. The presence of HCN channels introduces two distinct sets of changes in a neuronal compartment. First, they reduce intrinsic excitability (24–26, 45), and second, they introduce an inductive component to the impedance profile. Whereas the former reflects as a reduction in R_{in} and in the impedance amplitude across several frequencies, the latter manifests as resonance in impedance amplitude and a lead in impedance phase (28, 46, 47). The manifestation of the inductive component of HCN channels requires their (de)activation time constant be slower than that of the membrane time constant (28, 46, 47). Concordantly, an ideal method to test the relative contribution of intrinsic excitability vs. inductive component of the HCN channel to any measurement is to render the channel activation faster than the membrane time constant with an unaltered voltage-dependent gating profile. To address the question of what specific property of the HCN channel explains its impact on LFP and spike phases, we reduced the

(de)activation time constant of HCN channels (in what follows, we call them HCNFast channels) to around 7 ms [from $\sim 33 \text{ ms}$, at -65 mV (25)], thereby nullifying theta-frequency resonance and the inductive phase lead (Fig. S8A and B). As our analysis was confined to theta-modulated synaptic inputs (8 Hz), we matched neuronal excitability at 8 Hz at $\sim 250 \mu\text{m}$ from the soma to find appropriate values of $g_{\text{hF}}^{\text{Base}}$ (for the HCNFast channels) corresponding to each g_h^{Base} analyzed earlier (Fig. S8C–E). By doing this, we ensured that all distance- and voltage-dependent properties of HCNFast channels (including their reversal potential) and their impact on excitability were matched to the HCN counterparts, with the only exception that the presence of these channels would not introduce an inductive component onto the neuronal compartments.

Fast HCN Channels Revealed a Differential Role for Inductive and Excitability Changes Introduced by HCN Channels. To discern the roles of the inductive vs. the excitability component in altering

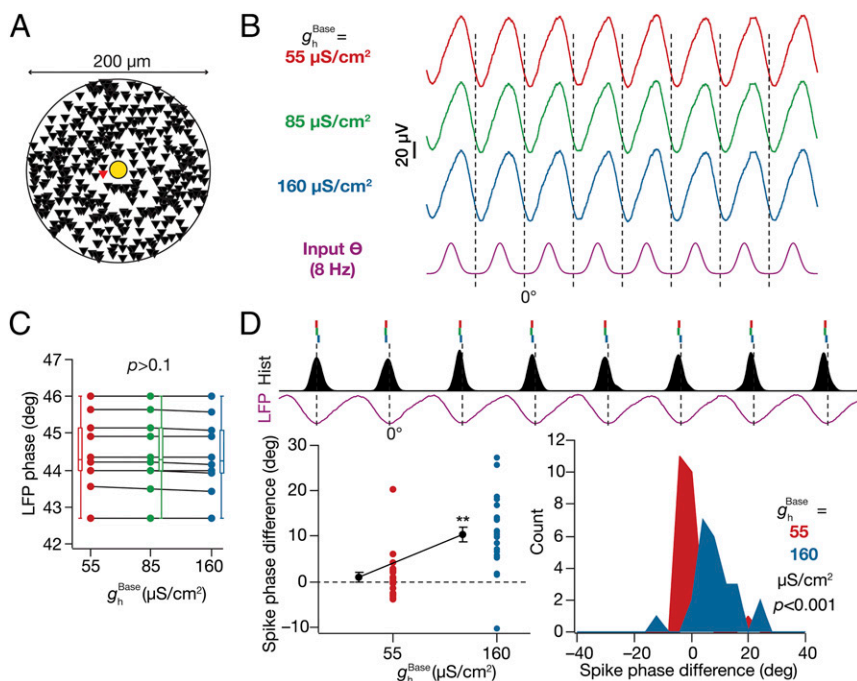


Fig. 5. Plasticity in HCN channels of an individual neuron shifted its spike phase. (A) Top view of the neuropil (Fig. 1A) depicting the location of the neuron undergoing plasticity (red), which is among the neurons closest to the electrode (yellow). (B) SP LFP (1 s), shown with reference to excitatory input θ , computed with g_h^{Base} for the chosen neuron set to one of three values: 55 μS/cm², 85 μS/cm², or 160 μS/cm². g_h^{Base} value for the other (439) neurons was set at the baseline value of 85 μS/cm². (C) SP LFP phase across cycles computed (with reference to excitatory input θ ; mean \pm SEM, 10 cycles) for corresponding traces shown in B. $P > 0.1$, Kruskal–Wallis test. (D, Top) Ticks representing spike timings of the single neuron undergoing plasticity with reference to SP LFP. Color codes of ticks correspond to the different values of g_h^{Base} (B). Histogram of spike timings of the other 23 neurons not undergoing plasticity is also shown (black). (D, Bottom Left) Cycle-matched difference between the spike phase of the chosen neuron computed with g_h^{Base} = 55 μS/cm² or 160 μS/cm² and the spike phase of the same neuron obtained with g_h^{Base} = 85 μS/cm². The different data points ($n = 24$; also mean \pm SEM) correspond to this spike-phase difference computed by placing different neurons at the specified location. $**P < 0.005$ (Student's t test on the null hypothesis of no spike-phase difference). (D, Bottom Right) Histogram of the spike-phase differences obtained across these 24 trials.

LFPs, we replaced HCN channels with their fast counterparts, computed SP LFP for different g_{hF}^{Base} values, and compared them with the LFPs computed with the corresponding (Fig. S8) g_h^{Base} values (Fig. 6A). Consequent to excitability not being altered by channel replacements (Fig. S8), we found that there was no significant difference in the LFP amplitudes (Fig. 6A). However, across strata, we found the lead observed in LFP phase in the presence of HCN channels was significantly reversed in the presence of HCNFast channels (Fig. 6B–D), suggesting that the inductive properties of HCN channels played a critical role in regulating the LFP phase lead. Further, we also noted the amount of HCNFast-induced reversal decreased with increase in conductance density (Fig. 6B–D), implying a role of changes in intrinsic excitability dominating in the presence of higher HCN conductances. When compared across HCNFast conductance values, LFP phase lead increased with an increase in HCNFast conductance (Fig. S8F), albeit with lower values for the phase lead in comparison to those obtained with HCN channels (compare Fig. 2B).

Next, we compared the population of spikes and their theta phases in the presence of HCN or HCNFast channels, across different conductance values (Fig. 6E–G). We observed that the presence of HCNFast channels reduced the spike-phase coherence compared to the presence of HCN channels (Fig. 6E and F), but with coherence values higher than those obtained with the passive case (Fig. 6F). Further, the amount of HCNFast-induced reduction in spike-phase coherence was higher for lower conductance values than for higher conductance values (Fig. 6F). Finally, the lag in theta phase of spikes introduced by HCN channels was reduced in the presence of HCNFast channels at lower HCN/HCNFast conductances, whereas when the conductance value increased, this lag remained intact (Fig. 6G).

To further assess the role of the (de)activation time constant of HCN channels in regulating LFPs and spike phase, we increased the (de)activation time constant to ~ 100 ms (HCNSlow) (Fig. S9A) and matched neuronal excitability at 8 Hz (Fig. S9B). This resulted in an increase in the impedance amplitude but at a lower resonance frequency (Fig. S9C) (28). As a direct consequence of the nonmonotonic changes in inductive phase lead with increase in the time constant (28), the LFP phase lead in-

troduced by HCN channels across different strata was partially reversed by their slower counterparts but not as much as by their faster counterparts (Fig. S9D and E). The spike phase obtained with HCNSlow channels, however, exhibited a lag that was larger than that in the presence of HCN channels, owing to the reduced impedance at the soma in the presence of the altered HCNSlow channels (Fig. S9F). Finally, the spike-phase coherence achieved with HCNSlow channels was lower than that in the presence of HCN channels (Fig. S9G–I).

How would neuronal spike phases and their dependencies on HCN/HCNFast channels change if we used LFP from a stratum other than the SP for computing spike phases? We noted a significant shift in the spike phase, apart from changes in the actual value of HCN-channel-induced phase lag in the spike phase, when we used LFPs from other strata as the reference (Fig. S10). Although these results emphasize the importance of electrode location with reference to the source-sink dipole for spike-phase computation, our overall conclusions on HCN channels and their inductive components remained intact. Next, to confirm the validity of our results for a frequency other than 8 Hz, we repeated our experiments (Figs. 2 and 6) with 5-Hz modulated synaptic inputs (Fig. S11) and found these results to be consistent with previous results.

In summary, these results suggested that the inductive lead induced by the presence of HCN channels and its regulation of transmembrane currents across the dendritic arbor critically contributed to the LFP phase lead, spike-phase lag, and enhancement of spike-phase coherence, especially at lower values of HCN conductance.

Discussion

The prime conclusion of our study is that HCN channels can significantly alter LFP phase and the associated theta-phase of neuronal firing, apart from enhancing spike-phase coherence. Importantly, we found that the ability of HCN channels to introduce an inductive phase lead in intracellular voltage responses to theta-modulated synaptic currents played a significant role in altering LFP and spike phases. These, in conjunction with our results on the implications for altering the kinetic and voltage-dependent properties, together emphasize a critical role for the

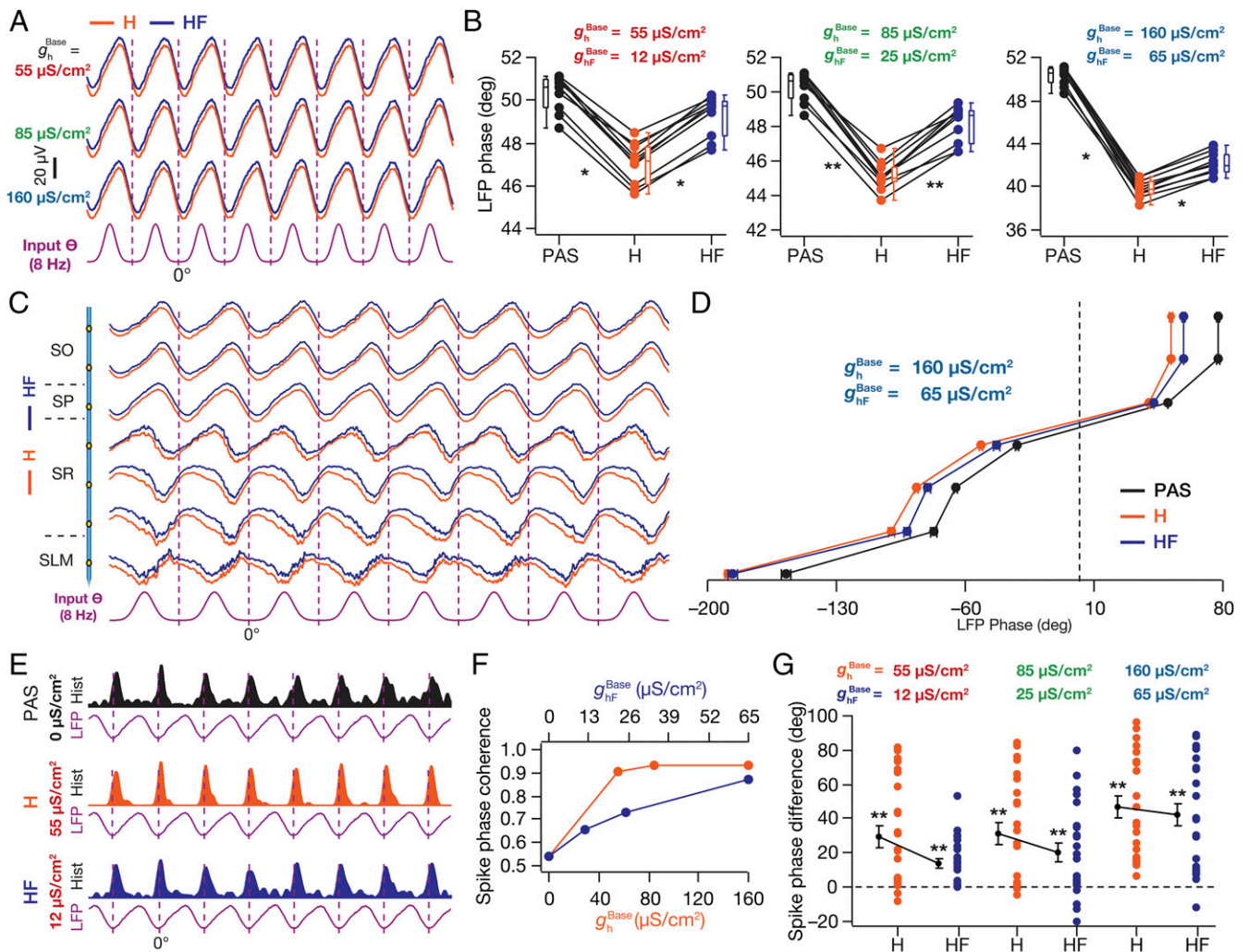


Fig. 6. The inductive component of HCN channels played a critical role in regulating LFP and spike phase as well as spike-phase jitter. (A) SP LFP traces (1 s) for different g_h^{Base} values (H) and corresponding g_{hF}^{Base} values (HF), shown with reference to the excitatory input θ (A, Bottom). (B) LFP phase (with reference to excitatory input θ ; mean \pm SEM, 10 cycles) across cycles plotted for three different values of g_h^{Base} and corresponding values of g_{hF}^{Base} . PAS, $g_h^{\text{Base}} = g_{hF}^{\text{Base}} = 0 \mu\text{S}/\text{cm}^2$; H, HCN channels inserted with the depicted value of g_h^{Base} ; HF, faster HCN channels inserted with the depicted value of g_{hF}^{Base} . (C) Normalized LFP traces (1 s) for different strata for $g_h^{\text{Base}} = 160 \mu\text{S}/\text{cm}^2$ and $g_{hF}^{\text{Base}} = 65 \mu\text{S}/\text{cm}^2$, with reference to excitatory input θ . (D) For each recording site (C), quantification of the LFP phase with reference to the excitatory input θ (mean \pm SEM, 10 cycles) for $g_h^{\text{Base}} = g_{hF}^{\text{Base}} = 0 \mu\text{S}/\text{cm}^2$ (PAS), $g_h^{\text{Base}} = 160 \mu\text{S}/\text{cm}^2$ (H), and its faster counterpart $g_{hF}^{\text{Base}} = 65 \mu\text{S}/\text{cm}^2$ (HF). (E) Population spike-time histograms (1 s) with corresponding SP LFP for $g_h^{\text{Base}} = g_{hF}^{\text{Base}} = 0 \mu\text{S}/\text{cm}^2$ (PAS), $g_h^{\text{Base}} = 55 \mu\text{S}/\text{cm}^2$ (H), and its faster counterpart $g_{hF}^{\text{Base}} = 12 \mu\text{S}/\text{cm}^2$ (HF). (F) Spike-phase coherence, C_ϕ , plotted as functions of g_h^{Base} and g_{hF}^{Base} . (G) Cycle-matched difference (8 cycles; mean \pm SEM) between the spike phase for the said g_h^{Base} (H) or the corresponding g_{hF}^{Base} (HF) value and the case where $g_h^{\text{Base}} = 0 \mu\text{S}/\text{cm}^2$ ($n = 24$ neurons for $g_h^{\text{Base}} = 85 \mu\text{S}/\text{cm}^2$ and $160 \mu\text{S}/\text{cm}^2$ and $g_{hF}^{\text{Base}} = 65 \mu\text{S}/\text{cm}^2$). (B) $*P < 0.05$, $**P < 0.005$ (Wilcoxon signed-rank test). (G) $**P < 0.005$ (Student's t test on the null hypothesis of no spike-phase difference).

unique voltage dependence and kinetic properties of HCN channels in regulating LFP and spike phases. Apart from demonstrating that our conclusions on HCN channels were robust to changes in several model parameters, we also report that synaptic scaling and excitatory–inhibitory phase difference could alter LFPs and spike phase, but not spike-phase coherence.

Phase Coding and Somatodendritic Ion Channels. LFPs have been referred to as the internal clocks for several neuronal circuits, and groups of cells have been shown to synchronize their spike timings to specific phases of the LFP, thus forming cell assemblies. The temporal/phase coding schema revolves around the fact that LFPs and specific timings of the spike with reference to these LFPs can convey information about the inputs that drove the spike, with behavioral relevance such as the animal's spatial location (4, 33, 35, 44). In this context, our results establish that the existence of and various forms of plasticity in HCN channels

and AMPA and GABA_A receptors could regulate the emergence and the evolution of the phase code in response to behavioral states, through state dependence and neuromodulation of their properties. The differences in spike phase introduced by plasticity/modulation in either HCN channels or the synaptic conductances are significant and large, spanning up to around 100° (Figs. 2 D and G; 3 F and J; 4 C, F, and I; 5 D; and 6 G). From the phase-coding perspective, especially with reference to theta–gamma coupling and gamma cell assemblies, the physiological and behavioral implications for such large differences in spike phases are enormous (4, 32, 33, 35, 44, 48–50). Together, our results argue for the incorporation of subthreshold-activated ion channels, their subcellular gradients, and their plasticity into the physiological and pathological studies on LFPs, phase coding, and neuronal cell assemblies. Our predictions on spike-phase coherence and about shifts in spike phases with reference to

LFPs could be experimentally tested by introducing specific pharmacological agents (that intracellularly alter channel properties) through an in vivo whole-cell patch pipette, in a configuration that involves awake-behaving extracellular and whole-cell recordings (51).

These very conclusions also imply that a group of cells can undergo specific forms of plasticity to synchronize their spike phases, thus configuring a new cell assembly. Apart from global changes, our results delineate specific roles for physiologically plausible localized changes in channel densities in altering the phase code and in allowing a neuron to switch cell assemblies by altering its spike phase, without significantly altering the external oscillator or its readout, the LFP (Fig. 5). Additionally, given such a multitude of mechanisms that can reconfigure phase codes and cell assemblies, these results also emphasize that the interpretation of experiments with pharmacological agents to block channels or with transgenic animals lacking genes encoding channel subunits should be done with utmost care. Such interpretation should account for our observation that upon blockade of channel currents, not only do spike timings change, but also the local reference LFP phase could change, thus resulting in a different reference point for the local temporal code. Finally, it is important that the interpretation of results with knockouts incorporates the differential impact of all compensatory mechanisms (52, 53) on LFPs and spike generation before attributing a specific role for a channel/subunit.

Limitations of the Analyses and Future Directions. First, similar to several previous studies (7, 8), our model assumes a homogenous and resistive extracellular field in arriving at the local field potentials. Although biophysical and experimental studies point to nonresistive components and nonhomogeneities in the extracellular fields, the impacts of these nonhomogeneities and nonresistive components are largely confined to higher frequencies (54–56). From these analyses, it stands to reason that the resistive and homogeneity assumptions are not debilitating for the conclusions drawn in our study where the range of frequencies is much lower, in the theta range.

Second, our study does not incorporate ephaptic coupling across neurons in the overall analysis (4, 57). Although it is clear that these ephaptic interactions, despite their small-amplitude deflections, can entrain action potentials at lower frequencies (57), the impact of such interactions on our conclusions is expected to be minimal. The reasons behind this are threefold: First, the presence of HCN channels did not significantly alter the amplitude of the LFPs (Figs. 2 and 3). Because volume conduction critically relies on the amplitude of the field signal, the impact of ephaptic interactions is not expected to change significantly in the presence or absence of HCN channels. Second, the open-field organization of hippocampal pyramidal neurons ensures that the somato-dendritic gradient in HCN channels is aligned with the source-sink dipole along the neuronal axis. If ephaptic coupling were present under a scenario where such alignment was absent, adjacent compartments from different neurons with huge differences in HCN-channel density would interact ephaptically, resulting in possible nullification of the impact of HCN channels on the LFP. However, given the alignment, our conclusions are not expected to change even in the presence of an additional distance-dependent ephaptic coupling across neurons with their

compartments endowed with similar gradients in HCN-channel density. Third, with reference to spike-phase coherence, although the presence of ephaptic interactions might further enhance the spike-phase coherence across neurons (57), our results are entirely related to the presence or absence of HCN channels. Specifically, the enhanced spike-phase coherence observed in the presence of HCN channels is a direct consequence of the ability of these channels to reduce the temporal window for spike-generating coincidence detection (38, 47) and is expected to be present even with ephaptic coupling in place.

Finally, our study was limited to HCN channels. However, our results call for the necessity to incorporate the wide array of somatodendritic subthreshold-activated channels (e.g., *A*-type K^+ , *T*-type Ca^{2+}), given their ability to regulate several aspects of neuronal physiology (15–17, 21, 58–62). Future studies should therefore focus on how the localization and targeting of these channel types are maintained across the somatodendritic arbor toward location-dependent regulation of LFPs, spike phases, and their coherence. In this context, it would be interesting to ask whether analogous LFPs and spike phases, and thereby analogous phase codes and cell assemblies, can be achieved with different channel/receptor combinations (58–60, 63).

Models and Methods

A detailed version of the simulated models and the methods employed is provided in *SI Models and Methods*. Briefly, we employed a forward modeling scheme with morphologically realistic neuronal models toward understanding the impact of active dendritic conductances on LFPs and spike theta phase of hippocampal pyramidal neurons. LFPs were constructed through line-source approximation (7, 8, 30, 31) of neuronal compartments from 440 (or 1,797 or 11,297; Fig. 3) morphologically realistic CA1 pyramidal neuron models. Two 3D reconstructions of a CA1 pyramidal neuron (*n123*, *ri04*) obtained from NeuroMorpho.Org (64–66) were employed (Fig. 1A and Fig. S3A) and were compartmentalized into 1,247 (*n123*)/1,351 (*ri04*) compartments. Somatodendritic passive, active, and synaptic parameters were set to match experimental data from somatodendritic recordings (26, 28, 29, 67, 68), with kinetics for the channels adopted from cell-attached recordings from soma and dendrites of hippocampal pyramidal neurons (25, 62, 69, 70). Specifically, the parameters were set to match normalization of somatic excitatory postsynaptic potential (EPSP) amplitudes, functional maps in input resistance, local and transfer resonance frequencies, and the synchronization frequency (Fig. 1B–E for *n123* and Fig. S3B–E for *ri04*). To account for the variability in theta-frequency LFP and in spike phase as the animal navigates in an arena (51), balanced rhythmic high-conductance state at theta frequency (default 8 Hz) was introduced through systematic randomization of the spatiotemporal activation of excitatory and inhibitory synapses distributed across the somatodendritic arbor. A phase difference (default 60°) was introduced in the perisomatic inhibitory inputs with reference to the predominantly dendritic excitatory inputs (34, 71, 72). All simulations were performed in the NEURON simulation environment (73) with an integration time constant of 25 μ s. Computation of line-source approximated (LSA) currents was performed using MATLAB R2011a (Mathworks), and analyses of LFP and spike phases were performed using MATLAB R2011a and Igor Pro (Wavemetrics). All statistical tests were performed using the R statistical package (www.r-project.org).

ACKNOWLEDGMENTS. The authors thank Dr. Daniel Johnston and members of the cellular neurophysiology laboratory for helpful discussions. This work was supported by the International Human Frontier Science Program Organization (R.N.), the Department of Biotechnology through the United States–India brain research collaborative program (R.N.), the Indian Institute of Science (R.N. and M.S.), and the Microsoft Research India PhD Fellowship Award (to M.S.).

- Katzner S, et al. (2009) Local origin of field potentials in visual cortex. *Neuron* 61(1): 35–41.
- Xing D, Yeh CI, Shapley RM (2009) Spatial spread of the local field potential and its laminar variation in visual cortex. *J Neurosci* 29(37):11540–11549.
- Kajikawa Y, Schroeder CE (2011) How local is the local field potential? *Neuron* 72(5): 847–858.
- Buzsáki G, Anastassiou CA, Koch C (2012) The origin of extracellular fields and currents—EEG, ECoG, LFP and spikes. *Nat Rev Neurosci* 13(6):407–420.
- Lindén H, et al. (2011) Modeling the spatial reach of the LFP. *Neuron* 72(5):859–872.
- Einevoll GT, Kayser C, Logothetis NK, Panzeri S (2013) Modelling and analysis of local field potentials for studying the function of cortical circuits. *Nat Rev Neurosci* 14(11): 770–785.
- Schomburg EW, Anastassiou CA, Buzsáki G, Koch C (2012) The spiking component of oscillatory extracellular potentials in the rat hippocampus. *J Neurosci* 32(34): 11798–11811.
- Reimann MW, et al. (2013) A biophysically detailed model of neocortical local field potentials predicts the critical role of active membrane currents. *Neuron* 79(2): 375–390.

9. Łęski S, Lindén H, Tetzlaff T, Pettersen KH, Einevoll GT (2013) Frequency dependence of signal power and spatial reach of the local field potential. *PLoS Comput Biol* 9(7): e1003137.
10. Ray S, Maunsell JH (2011) Different origins of gamma rhythm and high-gamma activity in macaque visual cortex. *PLoS Biol* 9(4):e1000610.
11. Waldert S, Lemon RN, Kraskov A (2013) Influence of spiking activity on cortical local field potentials. *J Physiol* 591(Pt 21):5291–5303.
12. Spruston N (2008) Pyramidal neurons: Dendritic structure and synaptic integration. *Nat Rev Neurosci* 9(3):206–221.
13. Nusser Z (2012) Differential subcellular distribution of ion channels and the diversity of neuronal function. *Curr Opin Neurobiol* 22(3):366–371.
14. Magee JC (2000) Dendritic integration of excitatory synaptic input. *Nat Rev Neurosci* 1(3):181–190.
15. Johnston D, Narayanan R (2008) Active dendrites: Colorful wings of the mysterious butterflies. *Trends Neurosci* 31(6):309–316.
16. Narayanan R, Johnston D (2012) Functional maps within a single neuron. *J Neurophysiol* 108(9):2343–2351.
17. Sjöström PJ, Rancz EA, Roth A, Häusser M (2008) Dendritic excitability and synaptic plasticity. *Physiol Rev* 88(2):769–840.
18. Beck H, Yaari Y (2008) Plasticity of intrinsic neuronal properties in CNS disorders. *Nat Rev Neurosci* 9(5):357–369.
19. Bernard C, Shah M, Johnston D (2007) Dendrites and disease. *Dendrites*, eds Stuart G, Spruston N, Häusser M (Oxford Univ Press, Oxford), 2nd Ed.
20. Lerche H, et al. (2013) Ion channels in genetic and acquired forms of epilepsy. *J Physiol* 591(Pt 4):753–764.
21. Remy S, Beck H, Yaari Y (2010) Plasticity of voltage-gated ion channels in pyramidal cell dendrites. *Curr Opin Neurobiol* 20(4):503–509.
22. Shah MM, Hammond RS, Hoffman DA (2010) Dendritic ion channel trafficking and plasticity. *Trends Neurosci* 33(7):307–316.
23. Brager DH, Akhavan AR, Johnston D (2012) Impaired dendritic expression and plasticity of h-channels in the *fmr1(-/y)* mouse model of fragile X syndrome. *Cell Rep* 1(3): 225–233.
24. Fan Y, et al. (2005) Activity-dependent decrease of excitability in rat hippocampal neurons through increases in I(h). *Nat Neurosci* 8(11):1542–1551.
25. Magee JC (1998) Dendritic hyperpolarization-activated currents modify the integrative properties of hippocampal CA1 pyramidal neurons. *J Neurosci* 18(19):7613–7624.
26. Narayanan R, Johnston D (2007) Long-term potentiation in rat hippocampal neurons is accompanied by spatially widespread changes in intrinsic oscillatory dynamics and excitability. *Neuron* 56(6):1061–1075.
27. Brager DH, Johnston D (2007) Plasticity of intrinsic excitability during long-term depression is mediated through mGluR-dependent changes in I(h) in hippocampal CA1 pyramidal neurons. *J Neurosci* 27(51):13926–13937.
28. Narayanan R, Johnston D (2008) The h channel mediates location dependence and plasticity of intrinsic phase response in rat hippocampal neurons. *J Neurosci* 28(22): 5846–5860.
29. Vaidya SP, Johnston D (2013) Temporal synchrony and gamma-to-theta power conversion in the dendrites of CA1 pyramidal neurons. *Nat Neurosci* 16(12):1812–1820.
30. Holt GR, Koch C (1999) Electrical interactions via the extracellular potential near cell bodies. *J Comput Neurosci* 6(2):169–184.
31. Gold C, Henze DA, Koch C, Buzsáki G (2006) On the origin of the extracellular action potential waveform: A modeling study. *J Neurophysiol* 95(5):3113–3128.
32. Wang XJ (2010) Neurophysiological and computational principles of cortical rhythms in cognition. *Physiol Rev* 90(3):1195–1268.
33. Buzsáki G (2010) Neural syntax: Cell assemblies, synapses, and readers. *Neuron* 68(3):362–385.
34. Buzsáki G (2002) Theta oscillations in the hippocampus. *Neuron* 33(3):325–340.
35. Moser EI, Kropff E, Moser MB (2008) Place cells, grid cells, and the brain's spatial representation system. *Annu Rev Neurosci* 31:69–89.
36. Mishra P, Narayanan R (2015) High-conductance states and A-type K⁺ channels are potential regulators of the conductance-current balance triggered by HCN channels. *J Neurophysiol* 113(1):23–43.
37. Pinsky PF, Rinzel J (1995) Synchrony measures for biological neural networks. *Biol Cybern* 73(2):129–137.
38. Das A, Narayanan R (2014) Active dendrites regulate spectral selectivity in location-dependent spike initiation dynamics of hippocampal model neurons. *J Neurosci* 34(4): 1195–1211.
39. Ratté S, Hong S, De Schutter E, Prescott SA (2013) Impact of neuronal properties on network coding: Roles of spike initiation dynamics and robust synchrony transfer. *Neuron* 78(5):758–772.
40. DiFrancesco D, Mangoni M (1994) Modulation of single hyperpolarization-activated channels (I_h) by cAMP in the rabbit sino-atrial node. *J Physiol* 474(3):473–482.
41. Pape HC (1996) Queer current and pacemaker: The hyperpolarization-activated cation current in neurons. *Annu Rev Physiol* 58:299–327.
42. Biel M, Wahl-Schott C, Michalakis S, Zong X (2009) Hyperpolarization-activated cation channels: From genes to function. *Physiol Rev* 89(3):847–885.
43. Narayanan R, Dougherty KJ, Johnston D (2010) Calcium store depletion induces persistent perisomatic increases in the functional density of h channels in hippocampal pyramidal neurons. *Neuron* 68(5):921–935.
44. Kayser C, Montemurro MA, Logothetis NK, Panzeri S (2009) Spike-phase coding boosts and stabilizes information carried by spatial and temporal spike patterns. *Neuron* 61(4): 597–608.
45. Gasparini S, DiFrancesco D (1997) Action of the hyperpolarization-activated current (I_h) blocker ZD 7288 in hippocampal CA1 neurons. *Pflügers Arch* 435(1):99–106.
46. Hutcheon B, Yarom Y (2000) Resonance, oscillation and the intrinsic frequency preferences of neurons. *Trends Neurosci* 23(5):216–222.
47. Remme MW, Rinzel J (2011) Role of active dendritic conductances in subthreshold input integration. *J Comput Neurosci* 31(1):13–30.
48. Buzsáki G, Wang XJ (2012) Mechanisms of gamma oscillations. *Annu Rev Neurosci* 35: 203–225.
49. Lisman JE, Jensen O (2013) The θ - γ neural code. *Neuron* 77(6):1002–1016.
50. Colgin LL, Moser EI (2010) Gamma oscillations in the hippocampus. *Physiology* 25(5): 319–329.
51. Harvey CD, Collman F, Dombeck DA, Tank DW (2009) Intracellular dynamics of hippocampal place cells during virtual navigation. *Nature* 461(7266):941–946.
52. Chen X, et al. (2010) Homeostatic regulation of synaptic excitability: Tonic GABA(A) receptor currents replace I(h) in cortical pyramidal neurons of HCN1 knock-out mice. *J Neurosci* 30(7):2611–2622.
53. Andrásfalvy BK, Makara JK, Johnston D, Magee JC (2008) Altered synaptic and non-synaptic properties of CA1 pyramidal neurons in Kv4.2 knockout mice. *J Physiol* 586(16):3881–3892.
54. Anastassiou CA, Montgomery SM, Barahona M, Buzsáki G, Koch C (2010) The effect of spatially inhomogeneous extracellular electric fields on neurons. *J Neurosci* 30(5): 1925–1936.
55. Bédard C, Kröger H, Destexhe A (2004) Modeling extracellular field potentials and the frequency-filtering properties of extracellular space. *Biophys J* 86(3):1829–1842.
56. Logothetis NK, Kayser C, Oeltermann A (2007) In vivo measurement of cortical impedance spectrum in monkeys: Implications for signal propagation. *Neuron* 55(5): 809–823.
57. Anastassiou CA, Perin R, Markram H, Koch C (2011) Ephaptic coupling of cortical neurons. *Nat Neurosci* 14(2):217–223.
58. Rathour RK, Narayanan R (2014) Homeostasis of functional maps in active dendrites emerges in the absence of individual channelostasis. *Proc Natl Acad Sci USA* 111(17): E1787–E1796.
59. Rathour RK, Narayanan R (2012) Inactivating ion channels augment robustness of subthreshold intrinsic response dynamics to parametric variability in hippocampal model neurons. *J Physiol* 590(Pt 22):5629–5652.
60. Anirudhan A, Narayanan R (2015) Analogous synaptic plasticity profiles emerge from disparate channel combinations. *J Neurosci* 35(11):4691–4705.
61. Ashhad S, Narayanan R (2013) Quantitative interactions between the A-type K⁺ current and inositol trisphosphate receptors regulate intraneuronal Ca²⁺ waves and synaptic plasticity. *J Physiol* 591(Pt 7):1645–1669.
62. Hoffman DA, Magee JC, Colbert CM, Johnston D (1997) K⁺ channel regulation of signal propagation in dendrites of hippocampal pyramidal neurons. *Nature* 387(6636): 869–875.
63. Marder E (2011) Variability, compensation, and modulation in neurons and circuits. *Proc Natl Acad Sci USA* 108(Suppl 3):15542–15548.
64. Pyapali GK, Sik A, Penttonen M, Buzsáki G, Turner DA (1998) Dendritic properties of hippocampal CA1 pyramidal neurons in the rat: Intracellular staining in vivo and in vitro. *J Comp Neurol* 391(3):335–352.
65. Ascoli GA, Donohue DE, Halavi M (2007) NeuroMorpho.Org: A central resource for neuronal morphologies. *J Neurosci* 27(35):9247–9251.
66. Golding NL, Mickus TJ, Katz Y, Kath WL, Spruston N (2005) Factors mediating powerful voltage attenuation along CA1 pyramidal neuron dendrites. *J Physiol* 568(Pt 1): 69–82.
67. Andrásfalvy BK, Magee JC (2001) Distance-dependent increase in AMPA receptor number in the dendrites of adult hippocampal CA1 pyramidal neurons. *J Neurosci* 21(23):9151–9159.
68. Magee JC, Cook EP (2000) Somatic EPSP amplitude is independent of synapse location in hippocampal pyramidal neurons. *Nat Neurosci* 3(9):895–903.
69. Magee JC, Johnston D (1995) Characterization of single voltage-gated Na⁺ and Ca²⁺ channels in apical dendrites of rat CA1 pyramidal neurons. *J Physiol* 487(Pt 1):67–90.
70. Migliore M, Hoffman DA, Magee JC, Johnston D (1999) Role of an A-type K⁺ conductance in the back-propagation of action potentials in the dendrites of hippocampal pyramidal neurons. *J Comput Neurosci* 7(1):5–15.
71. Klausberger T, et al. (2003) Brain-state- and cell-type-specific firing of hippocampal interneurons in vivo. *Nature* 421(6925):844–848.
72. Klausberger T, Somogyi P (2008) Neuronal diversity and temporal dynamics: The unity of hippocampal circuit operations. *Science* 321(5885):53–57.
73. Carnevale NT, Hines ML (2006) *The NEURON Book* (Cambridge Univ Press, Cambridge, UK).

Supporting Information

Sinha and Narayanan 10.1073/pnas.1419017112

SI Models and Methods

We employed a forward modeling scheme with morphologically realistic neuronal models toward understanding the impact of active dendritic conductances on local field potentials (LFPs) and spike theta phase of hippocampal pyramidal neurons. LFPs were constructed through line-source approximation (1–3) of neuronal compartments from 440 morphologically realistic CA1 pyramidal neuron models. Each neuron was rotated at an arbitrary angle, and the somata of these neurons spanned a cylindrical neuropil of 200 μm diameter and 40 μm height, with apical–basal orientation preserved across neurons (Fig. 1A). The number of neurons was chosen to match the observed density ($3.6 \times 10^5/\text{mm}^3$ in our simulations) in the CA1 region for the chosen volume of the cylindrical neuropil (4). We also performed sets of simulations with cylindrical neuropils of 400 μm and 1,000 μm diameter, with the height remaining the same at 40 μm (Fig. 3A–F). These neuropils contained a larger number of neurons, 1,797 and 11,297 in 400- μm and 1,000- μm neuropils, respectively, obtained from the same density of neurons as that of the 200- μm neuropil.

A virtual electrode with seven recording sites, with a 100- μm intersite distance, was placed at the center of the cylindrical neuropil to record LFPs from the different strata of the hippocampus (Fig. 1A). The seven-site recordings were chosen to reduce the computational complexity (see below) and to match with experimental recordings at different strata. It was ensured that the center coordinates of the soma of none of the neurons were placed within a cylinder of 15- μm radius from the center of the cylindrical neuropil. A three-dimensional reconstruction of a CA1 pyramidal neuron *n123* obtained from NeuroMorpho.org (5, 6) was employed (Fig. 1A). In simulations where we assessed the impact of morphological heterogeneity in the neuropil (Fig. 3G–J), we employed an additional three-dimensional reconstruction of a CA1 pyramidal neuron *ri04* obtained from NeuroMorpho.org (6, 7) (Fig. S3A) and distributed these two morphologies uniformly in a cylindrical neuropil of 200 μm diameter and 40 μm height (Fig. 3G). The default passive and active properties of either neuronal reconstruction (*n123* and *ri04*) were set such that several functional maps that exist across the neuronal topograph (Fig. 1C–E and Fig. S3C–E) matched their experimental counterparts and are outlined below (8–11).

Passive Properties. The specific membrane capacitance was kept uniform at 1 $\mu\text{F}/\text{cm}^2$ for the somatic and axonal compartments and was kept uniform at 1.8 $\mu\text{F}/\text{cm}^2$ throughout the rest of the neuronal topograph (7). Across compartments, we set the internal resistivity (R_a) uniformly to 150 $\Omega \cdot \text{cm}$ and 250 $\Omega \cdot \text{cm}$ for morphologies *n123* and *ri04*, respectively. For morphology *n123*, the specific membrane resistivity (R_m) along the somatoapical trunk varied nonuniformly to follow a sigmoidal dependence on radial distance (7, 8, 12, 13), x , of the compartment from the soma:

$$R_m(x) = 80 + \left(\frac{0.4 - 80}{1 + \exp((225 - x)/30)} \right) k\Omega \cdot \text{cm}^2. \quad [\text{S1}]$$

For morphology *ri04*, R_m as a function of x varied as

$$R_m(x) = 22 + \left(\frac{8 - 22}{1 + \exp((200 - x)/50)} \right) k\Omega \cdot \text{cm}^2. \quad [\text{S2}]$$

For apical oblique dendrites, the passive properties were set the same as the parent dendrite (on the trunk) that the oblique originated from. The passive properties for basal dendrites and axonal

compartments were the same as those for the somatic compartments. The models were compartmentalized into 1,247 (*n123*) and 1,351 (*ri04*) compartments, such that each compartment measured <10% of its space constant computed at 100 Hz (14).

Active Properties: Sodium and Potassium Channels. When inserted, densities of Na^+ and delayed rectifier K^+ channels were set to be uniform across the somatodendritic arbor (15, 16), with a five-fold increase in the density of Na^+ channels in the axonal initial segment (AIS) (17). There was no axonal compartment in *ri04*. The maximal conductance densities were $\bar{g}_{\text{Na}} = 20 \text{ mS}/\text{cm}^2$ (*n123*) and 8 mS/cm^2 (*ri04*), $\bar{g}_{\text{KDR}} = 1.4 \text{ mS}/\text{cm}^2$ (*n123*) and 5 mS/cm^2 (*ri04*), and $\bar{g}_{\text{Na}}(\text{AIS}) = 100 \text{ mS}/\text{cm}^2$ (*n123*). The kinetics for sodium and delayed rectifier potassium channels were adopted from experimental recordings from CA1 pyramidal neuronal soma and dendrites (15, 16, 18, 19). An additional gating variable was introduced for modeling the current through somatodendritic sodium channels, to incorporate slow recovery of these channels from inactivation (16, 18, 20),

$$I_{\text{Na}} = \bar{g}_{\text{Na}} m^3 h s (V_m - E_{\text{Na}}), \quad [\text{S3}]$$

where m and h represented the activation and inactivation gate, respectively, and s quantified the slow recovery from inactivation. To incorporate slow recovery from inactivation in dendritic channels, the steady-state value of s , s_∞ , was set as (18)

$$s_\infty = \frac{1 + F_{\text{rec}}^{\text{Na}} \exp((V_m + 58)/2)}{1 + \exp((V_m + 58)/2)}, \quad [\text{S4}]$$

where $F_{\text{rec}}^{\text{Na}}$ represented the recovery factor for sodium channels. If $F_{\text{rec}}^{\text{Na}} = 1$, $s_\infty = 1$, thus making the slow inactivation gate irrelevant. When $F_{\text{rec}}^{\text{Na}} = 0$, $s_\infty = (1 + \exp((V_m + 58)/2))^{-1}$, a sigmoid that represented the voltage dependence of the slow recovery from inactivation. Thus, the recovery of sodium channels from inactivation was slower if $F_{\text{rec}}^{\text{Na}}$ assumed lower values (in the range 0–1). The model for axonal Na^+ channels did not contain the additional inactivation gating variable s (20). The reversal potential for Na^+ and K^+ currents was 55 mV and –90 mV, respectively (18).

Active Properties: HCN Channels. The kinetics and voltage dependence of the current through HCN channels, I_h , were adopted from refs. 21–23,

$$I_h = \bar{g}_h s(V_m, t) (V_m - E_h), \quad [\text{S5}]$$

where \bar{g}_h denoted maximal HCN conductance; V_m , the membrane voltage; and E_h , the HCN-channel reversal potential, set at –30 mV. $s(V_m, t)$ controlled the voltage dependence and kinetics of the HCN channel and evolved based on first-order kinetics,

$$\frac{ds}{dt} = \frac{s_\infty - s}{\tau_h} \quad [\text{S6}]$$

$$s_\infty(V_m) = (1 + \exp((V_m - V_{1/2})/8))^{-1} \quad [\text{S7}]$$

$$\tau_{\text{HCN}}(V_m) = \frac{F_\tau \exp(0.033(V_m + 75))}{0.013(1 + \exp(0.083(V_m + 75)))}, \quad [\text{S8}]$$

where F_τ represented a factor that was employed in scaling the (de)activation time constant of HCN channels, without altering

its voltage dependence, and $V_{1/2}$ denoted the half-maximal activation voltage of the HCN channel.

When inserted, a sigmoidal gradient in HCN channel density (8, 21, 24) along the somatoapical trunk for morphology *n123* was set as

$$\bar{g}_h(x) = g_h^{\text{Base}} \left(1 + \frac{20}{1.0 + \exp((250 - x)/50)} \right) \mu\text{S}/\text{cm}^2. \quad [\text{S9}]$$

This gradient in HCN channel density and the associated passive properties ensured that R_{in} decreased from $\sim 60 \text{ M}\Omega$ at the soma to $\sim 20 \text{ M}\Omega$ at a trunk location $400 \mu\text{m}$ away from the soma (Fig. 1C). The local resonance frequency (f_{R} ; see below for details of measurements), measured at -65 mV (Fig. 1D), was $\sim 4 \text{ Hz}$ at the soma and $\sim 10 \text{ Hz}$ at a trunk location $300 \mu\text{m}$ away from the soma (8). Furthermore, transfer resonance frequency, f_{TR} , was normalized to $\sim 4\text{--}5 \text{ Hz}$ (Fig. 1D), and the synchronization frequency (11) was $\sim 8 \text{ Hz}$ for $g_h^{\text{Base}} = 85 \mu\text{S}/\text{cm}^2$ (Fig. 1E).

When HCN channels were included into the *ri04* reconstruction, the sigmoidal gradient along the somatoapical trunk was set as

$$\bar{g}_h(x) = g_h^{\text{Base}} \left(1 + \frac{120}{1.0 + \exp((275 - x)/50)} \right) \mu\text{S}/\text{cm}^2. \quad [\text{S10}]$$

This gradient in HCN channel density and the associated passive properties ensured that R_{in} decreased from $\sim 68 \text{ M}\Omega$ at the soma to $\sim 48 \text{ M}\Omega$ at a trunk location $250 \mu\text{m}$ away from the soma (Fig. S3C). The local resonance frequency (f_{R} ; see below for details of measurements), measured at -65 mV (Fig. S3D), was $\sim 4 \text{ Hz}$ at the soma and $\sim 10 \text{ Hz}$ at a trunk location $300 \mu\text{m}$ away from the soma (8). Furthermore, transfer resonance frequency, f_{TR} , was normalized to $\sim 4\text{--}7 \text{ Hz}$ (Fig. S3D), and the synchronization frequency (11) was $\sim 8 \text{ Hz}$ for $g_h^{\text{Base}} = 25 \mu\text{S}/\text{cm}^2$ (Fig. S3E). Variability in dendritic arborization and diameters implied that it was essential to independently adjust each active and passive property for the two morphologies to ensure that the different physiological measurements were set appropriately.

For both reconstructions, the half-maximal activation voltage was set to -82 mV for compartments $<100 \mu\text{m}$ away from the soma and hyperpolarized linearly up to -90 mV for compartments up to $300 \mu\text{m}$ away from the soma, beyond which it stayed at -90 mV (8, 21). The HCN-channel density and its half-maximal activation voltage, $V_{1/2}$, of any apical oblique dendrite were kept the same as those in the parent trunk dendrite that it originated from. For basal dendrites, HCN-channel density and kinetics were kept the same as those in the somatic compartments, and axonal compartments lacked HCN channels. Together, we ensured that the somatodendritic heterogeneities of ion channels and associated measurements were appropriately accounted for in each of the two morphologies employed in our study.

To assess the role of HCN-channel plasticity on LFPs, we increased or decreased the HCN-channel density globally across the somatodendritic arbor of all neurons to either increase (8) or decrease (25) somatic f_{R} by $\sim 20\%$, respectively. We accomplished this by retaining the normalized somatodendritic gradient of HCN channels to be the same, while altering only the base (somatic) value of HCN-channel density, g_h^{Base} . HCN channels are gated by cyclic nucleotides like cAMP and there is evidence that such gating is HCN subtype dependent (26, 27). Also, HCN subtype-dependent shifts in $V_{1/2}$ of these channels have been reported (28). To study the effect of shifts in the $V_{1/2}$ of HCN channels on LFP and spike phase, we also changed the $V_{1/2}$ of HCN channels by $\pm 5 \text{ mV}$ throughout the neuron. To study the effect of subtype-dependent (28–34) changes in HCN-channel time constant (τ_{HCN} ; Eq. S8) on LFPs, the scaling factor F_{τ} was increased to 3 (for HCNSlow channels) or decreased to 0.2 (for HCNFast channels) from its default value of 1 (Fig. 6 and Figs. S8–S11).

Synaptic Stimulation. Fifty excitatory synapses containing AMPA receptors (localized to apical dendritic compartments $50\text{--}300 \mu\text{m}$ from the soma) and 25 inhibitory synapses containing GABA_A receptors ($0\text{--}100 \mu\text{m}$ from the soma) were randomly distributed by picking location values from uniform distributions in that range. Spike timings of incoming inputs were Gaussian modulated for both excitatory and inhibitory inputs, with a standard deviation set at one-eighth and one-fifth of the 8-Hz [the dominant theta frequency in the hippocampal region (35)] oscillatory cycle for the excitatory and inhibitory inputs, respectively. The inhibitory inputs were set to have a 60° phase lead with reference to the excitatory inputs (36–38). Specifically, the number of action potentials received by an excitatory synapse was governed by the distribution (2)

$$N_e(t) = A_e \exp \left(-\frac{(\text{mod}(t, T_\theta) - T_\theta/2)^2}{2\sigma_e^2} \right) \quad [\text{S11}]$$

and those received by an inhibitory synapse were governed by

$$N_i(t) = A_i \exp \left(-\frac{(\text{mod}(t + \phi_{\text{gin}}, T_\theta) - T_\theta/2)^2}{2\sigma_i^2} \right), \quad [\text{S12}]$$

where T_θ represents the time period of the theta oscillations (125 ms for 8 Hz), $\sigma_i = T_\theta/5$, $\sigma_e = T_\theta/8$, mod represents the modulo function, and ϕ_{gin} in $N_i(t)$ constitutes the 60° phase lead in inhibitory synaptic inputs. Scaling factors A_e and A_i are set at unity. Although all excitatory and inhibitory synapses followed their respective distributions above, individual synaptic timings were independent and randomized with a constraint on the distribution. Whereas the choice of frequency was driven by experimental theta frequency ranges, the phase lead in inhibitory neurons was modeled to account for the theta phase of basket cells in the CA1 region (35, 37, 38). To study the effect of changes in the arrival phase difference between excitation and inhibition, we also changed the value of ϕ_{gin} to -60° and 0° in two sets of simulations (Fig. 4 and Fig. S6).

The reversal potential for the AMPAR currents was 0 mV and for the GABA_AR currents was -80 mV . Synaptic currents were modeled as double exponentials with the rise time constant set at 0.1 ms and the decay time constant set at 5 ms for both AMPAR and GABA_AR currents. AMPAR conductance at all excitatory synapses was set such that the peak “unitary” somatic voltage (v_{uEPSP}) was fixed irrespective of the location of the synapse (39, 40). This was accomplished by finding the minimum AMPA receptor conductance required at each location along the apical dendritic arbor (Fig. 1B for *n123*; Fig. S3B for *ri04*) for achieving a peak somatic EPSP value of v_{uEPSP} (41). The default value of v_{uEPSP} was $4.8 \mu\text{V}$. Note that this v_{uEPSP} is only a relative measure of excitatory output, as the overall inputs and the consequent output are driven by the conductance of the AMPA receptors, the value of A_e in the excitatory theta input (Eq. S11), and the spatiotemporal distribution of synapses. The default values of inhibitory synaptic conductances were set to 100 pS for *n123* and 200 pS for *ri04* such that a sufficient number of spikes could be triggered at the soma with given AMPAR conductances.

To study the effects of excitatory synaptic scaling (Fig. 4 and Fig. S4), we changed v_{uEPSP} to a higher or lower value by scaling the AMPAR conductance. The impact of inhibitory synaptic scaling (Fig. 4 and Fig. S5) was assessed by changing the GABA_AR conductance to a lower value (50 pS) or a higher value (200 pS). To assess the impact of variability in the reversal potential of GABA_AR, especially of shunting inhibition (42–44), in a set of simulations (Fig. S7), we changed the GABA_AR reversal potential to -65 mV (which is resting membrane potential) and -70 mV

from its default value of -80 mV. When these sensitivity analyses were performed, all other parameters were set to default values.

LFP Calculations. To assess the specific roles of different model components on the LFPs, simulations were performed across different parametric values for channel and receptor densities. Simulations were performed for $n = 25/23$ ($n123/ri04$) different trials for each parametric variation; synaptic locations and their timings randomly varied across different trials. Simulations were trial matched across parametric changes so that paired comparisons could be performed across parametric variations. The randomization of synaptic localization and timings effectively accounted for the noise and the variability in spike phase observed under in vivo conditions (45). Specifically, this systematic randomization of the spatiotemporal activation profile replicated noise and variability in spike phase and timing, whereby there were theta cycles where there were multiple spikes (e.g., Fig. 1H and Fig. S3H) and cycles where there were no spikes (e.g., Fig. S3H). These apart, such systematic randomization ensured that there was cycle-to-cycle variability in LFP and spike phase across parametric configurations, which is represented as statistical variability in these quantities across all figures (e.g., Figs. 1F–H and 2A, B, D, E, and G).

The total currents, computed as the sum of capacitive, passive, active, and synaptic currents, from all the compartments of these morphologically realistic models for various combinations of passive and active parameters were recorded for each of the n trials. The number of trials was set at 25 to reduce computational load (2), and line-source approximated (LSA) currents from these 25 neurons were uniformly distributed across the population of neurons ($N_n = 440, 1,797$, and $11,297$ for three different neuropil sizes) that contributed to LFPs. For the analysis of morphological heterogeneity, 10 trials of $ri04$ and 13 trials of $n123$ were uniformly distributed over 226 and 214 neurons, respectively. LFP at each of the seven recording sites, e , was then computed from the distance-scaled LSA currents (I_{ij}) from all line segments making up the morphology ($N_i = 5,160$ for $n123$ and $N_i = 9,814$ for $ri04$) of all neurons ($N_n = 440, 1,797$, or $11,297$) in the neuropil as (1, 2, 46–49)

$$V_e = \sum_{i=1}^{N_n} \sum_{j=1}^{N_i} \frac{\rho I_{ij}}{4\pi l_{ij}} \log \frac{\sqrt{h_{ij}^2 + r_{ij}^2} - h_{ij}}{\sqrt{s_{ij}^2 + r_{ij}^2} - s_{ij}}, \quad [S13]$$

where, the extracellular resistivity, ρ , was kept uniform and was set to $3.33 \Omega \cdot \text{m}$, and the other geometry-related parameters h_{ij} , r_{ij} , and s_{ij} for each line segment of each neuron were computed with reference to a given recording site as follows (1, 2, 46, 50) (Fig. 1A). For a given recording site e , a perpendicular was dropped from the point to line segment j of length l_{ij} in neuron i . The radial separation, r_{ij} , was computed as the length of this perpendicular, and the perpendicular separation, h_{ij} , was calculated as the nearest distance between the line segment and the dropped perpendicular. s_{ij} was then set as $l_{ij} + h_{ij}$ (Fig. 1A). As in standard conventions, locations where the net current was outward led to the formation of sources, whereas sinks were at locations where the net current was inward. LFPs were computed for all seven recording sites (e.g., Fig. 1F). To remove the spiking component from the LFP (2) and measure the LFP resulting from subthreshold contributions, the conductances of sodium and delayed rectifier potassium channels were set to zero. Ephaptic coupling was not accounted for (49, 51).

It should be noted that the computational complexity involved in obtaining LFPs at each of the seven electrode sites and for each parametric combination was enormous. Specifically, each of the seven electrode sites required that we incorporate the 1,247 compartments with 5,160 line segments of each of the 440 (or

1,797/11,297; Fig. 3) neurons (accounting for distance of the electrode site from the compartment), with each compartment accounted for by several transmembrane currents, each of which evolves as a function of time for around 1.5 s (12 cycles of 8-Hz theta) of simulation time.

Computation of LFP Amplitude and Phase. LFP amplitudes (Fig. 3B) were computed as $\sqrt{((8/T) \int_0^T f(t)^2 dt)}$, where $f(t)$ represented the LFP and T was 1 s. For computing the per-neuron contribution to the LFP from a population of neurons (Fig. 3B), we divided the computed LFP amplitude by the number of neurons in the population under consideration.

LFP phase was calculated with reference to the excitatory input theta (Eq. S11). LFP phase was calculated across 10 cycles (6 cycles for Fig. S11 and 8 cycles for Fig. 4G, Right, SLM layer). For comparison of the SP LFP across parametric values the distributions of these 10 different phase values were used (Fig. 2B). Consistent with prior conventions, negative and positive phase differences meant a lead and a lag, respectively, and held for both LFP and spike time phases (discussed below). Normalized LFP traces were employed at instances where phase differences and not amplitude differences were emphasized. Unless otherwise stated, the trough of the excitatory input theta (Eq. S11) was taken to be the reference at 0° for computing phase differences between LFPs in the different strata and across different passive, active, and synaptic parametric variations.

Computation of Spike Phase and Its Coherence. Spike timings were computed from intracellular traces recorded at the soma of the model neuron across each of the n trials, when Na^+ and delayed rectifier K^+ channels were present. The point at which the rising phase of an action potential crossed -10 mV was taken as the timing for a somatic spike of a neuron. Unless otherwise specified (e.g., Fig. S10), spike phase was computed by comparing neuronal spike timings with reference to corresponding stratum pyramidale (SP) LFPs, considering the trough to be at 0° of the LFP (Fig. 1G and H). To account for cycle-to-cycle variability, the phase of the first spike across eight cycles (five cycles for Fig. S11) of the LFP was computed (Fig. 1G) and these eight values were employed for further analyses. In graphs that represent spike phase differences across different trials (e.g., Fig. 2D), each marker represents the mean (computed for the eight cycles) cycle-matched spike-phase difference for a given trial (say $\varphi_{1-\varphi_n}$; the number of trials $n = 25$). Trials where the neuron had less than three spikes over eight cycles were discarded from the analysis (cases where $n < 25$ are mentioned in the figure legends). Also plotted in these graphs are markers with error bars that represent the mean \pm SEM computed across these n trials (i.e., statistics on the values $\varphi_{1-\varphi_n}$).

Spike-phase coherence, C_Φ , defined on the phase of spikes with reference to SP LFP (Fig. 2C), was computed on the vector of all spike phases across different neurons/trials (52, 53). Let $\Phi = (\phi_1 \dots \phi_n)$, $\phi_i \in [0, 1]$ be a vector of phases from N neurons/trials. We defined $\zeta(\Phi) = \exp(j\Phi)$, $j = \sqrt{-1}$, and computed spike-phase coherence from the variance of the vector $\zeta(\Phi)$ of complex numbers (52, 53) as

$$C_\Phi = 1 - \frac{1}{n} \sum_{i=1}^n |\zeta_i(\Phi) - \bar{\zeta}(\Phi)|^2, \quad [S14]$$

where $\bar{\zeta}(\Phi) = (1/n) \sum_{i=1}^n \zeta_i(\Phi)$. By this definition, C_Φ would be 0 for a uniform distribution of phases and would be 1 if there exists a phase preference exclusively for a specific phase.

Computational and Measurement Details. All simulations were performed in the NEURON simulation environment (14), at -65 mV

and 34° C, with an integration time constant of 25 μ s. Computation of LSA currents was performed using MATLAB R2011a (Mathworks), and analyses of LFP and spike phases were performed using MATLAB R2011a and Igor Pro (Wavemetrics). The software for computing LFPs was derived from the literature (ModelDB accession no. 84589) on modeling extracellular action potentials (1, 2, 46, 50), with modifications performed to incorporate gradients in ion channels to impose specific somatodendritic functional maps mentioned above.

R_{in} at a given somatodendritic location was measured as the ratio of the local steady-state voltage response to a local injection of a hyperpolarizing current pulse of amplitude ~ 100 pA. Impedance was measured using a chirp stimulus, which was a sinusoidal current wave with constant amplitude (100 pA), with frequency linearly increasing from 0 Hz to 25 Hz in 25 s. Two types of impedance measurements were performed (8, 9, 11, 54): local, $Z(f)$, and transfer, $Z_{TR}(f)$. For local measurements, the voltage response was measured at the same location where the chirp stimulus was injected, whereas for transfer measurements,

the voltage response was recorded at the soma. The frequencies at which the local and transfer impedance amplitudes reached their maximum were defined as f_R and f_{TR} , respectively. The phases of $Z(f)$ and $Z_{TR}(f)$ were represented by $\phi(f)$ and $\phi_{TR}(f)$, respectively.

Statistical Tests. All statistical tests were performed using the R statistical package (www.r-project.org). As simulations across different parametric variabilities were trial matched across each of the 25 trials (23 trials for Fig. 3 G–J), we performed paired statistical tests across sets of simulations performed under different parametric distributions. For all nonparametric statistical tests, variability in data was represented as median with quartiles. We performed a Kruskal–Wallis test for comparing more than two distributions and a Wilcoxon signed-rank test for comparing two distributions. We performed a paired Student's t test for comparing spike-phase differences. For all parametric statistical tests, variability in data was represented as mean with SEM. The confidence level was set to 95%. P values for all statistical tests are specified in the corresponding figures.

- Holt GR, Koch C (1999) Electrical interactions via the extracellular potential near cell bodies. *J Comput Neurosci* 6(2):169–184.
- Schomburg EW, Anastassiou CA, Buzsáki G, Koch C (2012) The spiking component of oscillatory extracellular potentials in the rat hippocampus. *J Neurosci* 32(34):11798–11811.
- Reimann MW, et al. (2013) A biophysically detailed model of neocortical local field potentials predicts the critical role of active membrane currents. *Neuron* 79(2):375–390.
- Boss BD, Turlejski K, Stanfield BB, Cowan WM (1987) On the numbers of neurons in fields CA1 and CA3 of the hippocampus of Sprague-Dawley and Wistar rats. *Brain Res* 406(1–2):280–287.
- Pyapali GK, Sik A, Penttonen M, Buzsáki G, Turner DA (1998) Dendritic properties of hippocampal CA1 pyramidal neurons in the rat: Intracellular staining in vivo and in vitro. *J Comp Neurol* 391(3):335–352.
- Ascoli GA, Donohue DE, Halavi M (2007) NeuroMorpho.Org: A central resource for neuronal morphologies. *J Neurosci* 27(35):9247–9251.
- Golding NL, Mickus TJ, Katz Y, Kath WL, Spruston N (2005) Factors mediating powerful voltage attenuation along CA1 pyramidal neuron dendrites. *J Physiol* 568(Pt 1):69–82.
- Narayanan R, Johnston D (2007) Long-term potentiation in rat hippocampal neurons is accompanied by spatially widespread changes in intrinsic oscillatory dynamics and excitability. *Neuron* 56(6):1061–1075.
- Narayanan R, Johnston D (2008) The h channel mediates location dependence and plasticity of intrinsic phase response in rat hippocampal neurons. *J Neurosci* 28(22):5846–5860.
- Narayanan R, Johnston D (2012) Functional maps within a single neuron. *J Neurophysiol* 108(9):2343–2351.
- Vaidya SP, Johnston D (2013) Temporal synchrony and gamma-to-theta power conversion in the dendrites of CA1 pyramidal neurons. *Nat Neurosci* 16(12):1812–1820.
- Narayanan R, Dougherty KJ, Johnston D (2010) Calcium store depletion induces persistent perisomatic increases in the functional density of h channels in hippocampal pyramidal neurons. *Neuron* 68(5):921–935.
- Poirazi P, Brannon T, Mel BW (2003) Pyramidal neuron as two-layer neural network. *Neuron* 37(6):989–999.
- Carnevale NT, Hines ML (2006) *The NEURON Book* (Cambridge Univ Press, Cambridge, UK).
- Magee JC, Johnston D (1995) Characterization of single voltage-gated Na⁺ and Ca²⁺ channels in apical dendrites of rat CA1 pyramidal neurons. *J Physiol* 487(Pt 1):67–90.
- Hoffman DA, Magee JC, Colbert CM, Johnston D (1997) K⁺ channel regulation of signal propagation in dendrites of hippocampal pyramidal neurons. *Nature* 387(6636):869–875.
- Fleiderovich IA, Lasser-Ross N, Gutnick MJ, Ross WN (2010) Na⁺ imaging reveals little difference in action potential-evoked Na⁺ influx between axon and soma. *Nat Neurosci* 13(7):852–860.
- Migliore M, Hoffman DA, Magee JC, Johnston D (1999) Role of an A-type K⁺ conductance in the back-propagation of action potentials in the dendrites of hippocampal pyramidal neurons. *J Comput Neurosci* 7(1):5–15.
- Klee R, Ficker E, Heinemann U (1995) Comparison of voltage-dependent potassium currents in rat pyramidal neurons acutely isolated from hippocampal regions CA1 and CA3. *J Neurophysiol* 74(5):1982–1995.
- Colbert CM, Magee JC, Hoffman DA, Johnston D (1997) Slow recovery from inactivation of Na⁺ channels underlies the activity-dependent attenuation of dendritic action potentials in hippocampal CA1 pyramidal neurons. *J Neurosci* 17(17):6512–6521.
- Magee JC (1998) Dendritic hyperpolarization-activated currents modify the integrative properties of hippocampal CA1 pyramidal neurons. *J Neurosci* 18(19):7613–7624.
- Pooslos NP, Migliore M, Johnston D (2002) Pharmacological upregulation of h-channels reduces the excitability of pyramidal neuron dendrites. *Nat Neurosci* 5(8):767–774.
- Gasparini S, Migliore M, Magee JC (2004) On the initiation and propagation of dendritic spikes in CA1 pyramidal neurons. *J Neurosci* 24(49):11046–11056.
- Lörincz A, Notomi T, Tamás G, Shigemoto R, Nusser Z (2002) Polarized and compartment-dependent distribution of HCN1 in pyramidal cell dendrites. *Nat Neurosci* 5(11):1185–1193.
- Brager DH, Johnston D (2007) Plasticity of intrinsic excitability during long-term depression is mediated through mGluR-dependent changes in I(h) in hippocampal CA1 pyramidal neurons. *J Neurosci* 27(51):13926–13937.
- Zolles G, et al. (2009) Association with the auxiliary subunit PEX5R/Trip8b controls responsiveness of HCN channels to cAMP and adrenergic stimulation. *Neuron* 62(6):814–825.
- DiFrancesco D, Mangoni M (1994) Modulation of single hyperpolarization-activated channels (I_h) by cAMP in the rabbit sino-atrial node. *J Physiol* 474(3):473–482.
- Dougherty KA, et al. (2013) Differential expression of HCN subunits alters voltage-dependent gating of h-channels in CA1 pyramidal neurons from dorsal and ventral hippocampus. *J Neurophysiol* 109(7):1940–1953.
- Ishii TM, Takano M, Ohmori H (2001) Determinants of activation kinetics in mammalian hyperpolarization-activated cation channels. *J Physiol* 537(Pt 1):93–100.
- Ishii TM, Takano M, Xie LH, Noma A, Ohmori H (1999) Molecular characterization of the hyperpolarization-activated cation channel in rabbit heart sinoatrial node. *J Biol Chem* 274(18):12835–12839.
- Ludwig A, et al. (1999) Two pacemaker channels from human heart with profoundly different activation kinetics. *EMBO J* 18(9):2323–2329.
- Seifert R, et al. (1999) Molecular characterization of a slowly gating human hyperpolarization-activated channel predominantly expressed in thalamus, heart, and testis. *Proc Natl Acad Sci USA* 96(16):9391–9396.
- Stieber J, Stöckl G, Herrmann S, Hassfurth B, Hofmann F (2005) Functional expression of the human HCN3 channel. *J Biol Chem* 280(41):34635–34643.
- Santoro B, et al. (2000) Molecular and functional heterogeneity of hyperpolarization-activated pacemaker channels in the mouse CNS. *J Neurosci* 20(14):5264–5275.
- Buzsáki G (2002) Theta oscillations in the hippocampus. *Neuron* 33(3):325–340.
- Csicsvari J, Hirase H, Czurkó A, Mamiya A, Buzsáki G (1999) Oscillatory coupling of hippocampal pyramidal cells and interneurons in the behaving rat. *J Neurosci* 19(1):274–287.
- Klausberger T, et al. (2003) Brain-state- and cell-type-specific firing of hippocampal interneurons in vivo. *Nature* 421(6925):844–848.
- Klausberger T, Somogyi P (2008) Neuronal diversity and temporal dynamics: The unity of hippocampal circuit operations. *Science* 321(5885):53–57.
- Smith MA, Ellis-Davies GC, Magee JC (2003) Mechanism of the distance-dependent scaling of Schaffer collateral synapses in rat CA1 pyramidal neurons. *J Physiol* 548(Pt 1):245–258.
- Andrasfalvy BK, Magee JC (2001) Distance-dependent increase in AMPA receptor number in the dendrites of adult hippocampal CA1 pyramidal neurons. *J Neurosci* 21(23):9151–9159.
- Narayanan R, Chattarji S (2010) Computational analysis of the impact of chronic stress on intrinsic and synaptic excitability in the hippocampus. *J Neurophysiol* 103(6):3070–3083.
- Rall W (1977) Core conductor theory and cable properties of neurons. *Handbook of Physiology. The Nervous System. Cellular Biology of Neurons*, ed Kandel ER (Am Physiol Soc, Bethesda), Vol 1, pp 39–97.
- Staley KJ, Mody I (1992) Shunting of excitatory input to dentate gyrus granule cells by a depolarizing GABA_A receptor-mediated postsynaptic conductance. *J Neurophysiol* 68(1):197–212.
- Ben-Ari Y (2002) Excitatory actions of gaba during development: The nature of the nurture. *Nat Rev Neurosci* 3(9):728–739.
- Harvey CD, Collman F, Dombeck DA, Tank DW (2009) Intracellular dynamics of hippocampal place cells during virtual navigation. *Nature* 461(7266):941–946.
- Gold C, Henze DA, Koch C, Buzsáki G (2006) On the origin of the extracellular action potential waveform: A modeling study. *J Neurophysiol* 95(5):3113–3128.
- Rall W, Shepherd GM (1968) Theoretical reconstruction of field potentials and dendrodendritic synaptic interactions in olfactory bulb. *J Neurophysiol* 31(6):884–915.
- Einav GT, Kayser C, Logothetis NK, Panzeri S (2013) Modelling and analysis of local field potentials for studying the function of cortical circuits. *Nat Rev Neurosci* 14(11):770–785.

49. Buzsáki G, Anastassiou CA, Koch C (2012) The origin of extracellular fields and currents—EEG, ECoG, LFP and spikes. *Nat Rev Neurosci* 13(6):407–420.
50. Gold C, Henze DA, Koch C (2007) Using extracellular action potential recordings to constrain compartmental models. *J Comput Neurosci* 23(1):39–58.
51. Anastassiou CA, Perin R, Markram H, Koch C (2011) Ephaptic coupling of cortical neurons. *Nat Neurosci* 14(2):217–223.

52. Pinsky PF, Rinzel J (1995) Synchrony measures for biological neural networks. *Biol Cybern* 73(2):129–137.
53. Strogatz S, Mirollo R (1991) Stability of incoherence in a population of coupled oscillators. *J Stat Phys* 63:613–636.
54. Hutcheon B, Yarom Y (2000) Resonance, oscillation and the intrinsic frequency preferences of neurons. *Trends Neurosci* 23(5):216–222.

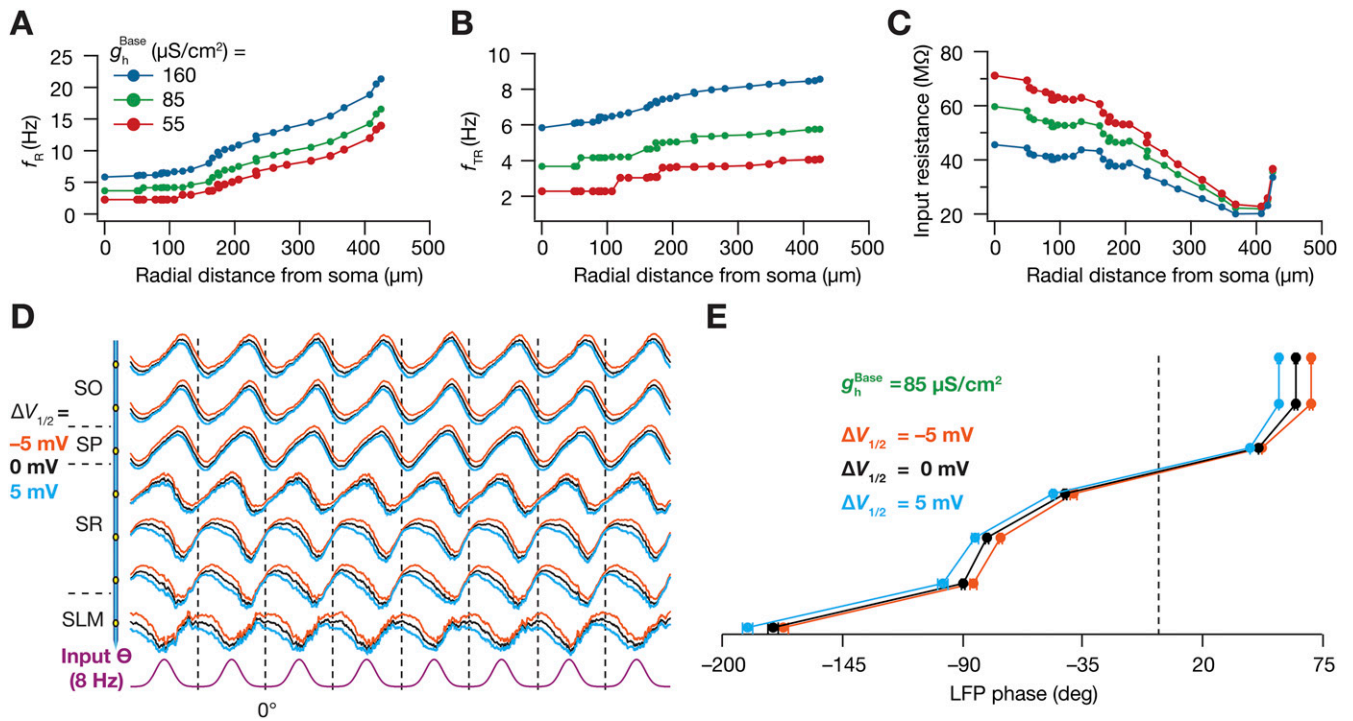


Fig. S1. Global HCN plasticity in conductance or in half-maximal activation voltage. (A–C) Functional maps of (A) local resonance frequency (f_r), (B) transfer resonance frequency (f_{TR}), and (C) input resistance (R_{in}) along the somatoapical trunk for three different g_h^{Base} values. (D) Normalized LFP traces (1 s) for different strata with $g_h^{\text{Base}} = 85 \mu\text{S}/\text{cm}^2$ for baseline $V_{1/2}$ ($\Delta V_{1/2} = 0 \text{ mV}$), hyperpolarized $V_{1/2}$ ($\Delta V_{1/2} = -5 \text{ mV}$), and depolarized $V_{1/2}$ ($\Delta V_{1/2} = +5 \text{ mV}$). (E) LFP phase with reference to the excitatory input θ (mean \pm SEM, 10 cycles) for different $\Delta V_{1/2}$ values for all recording sites.

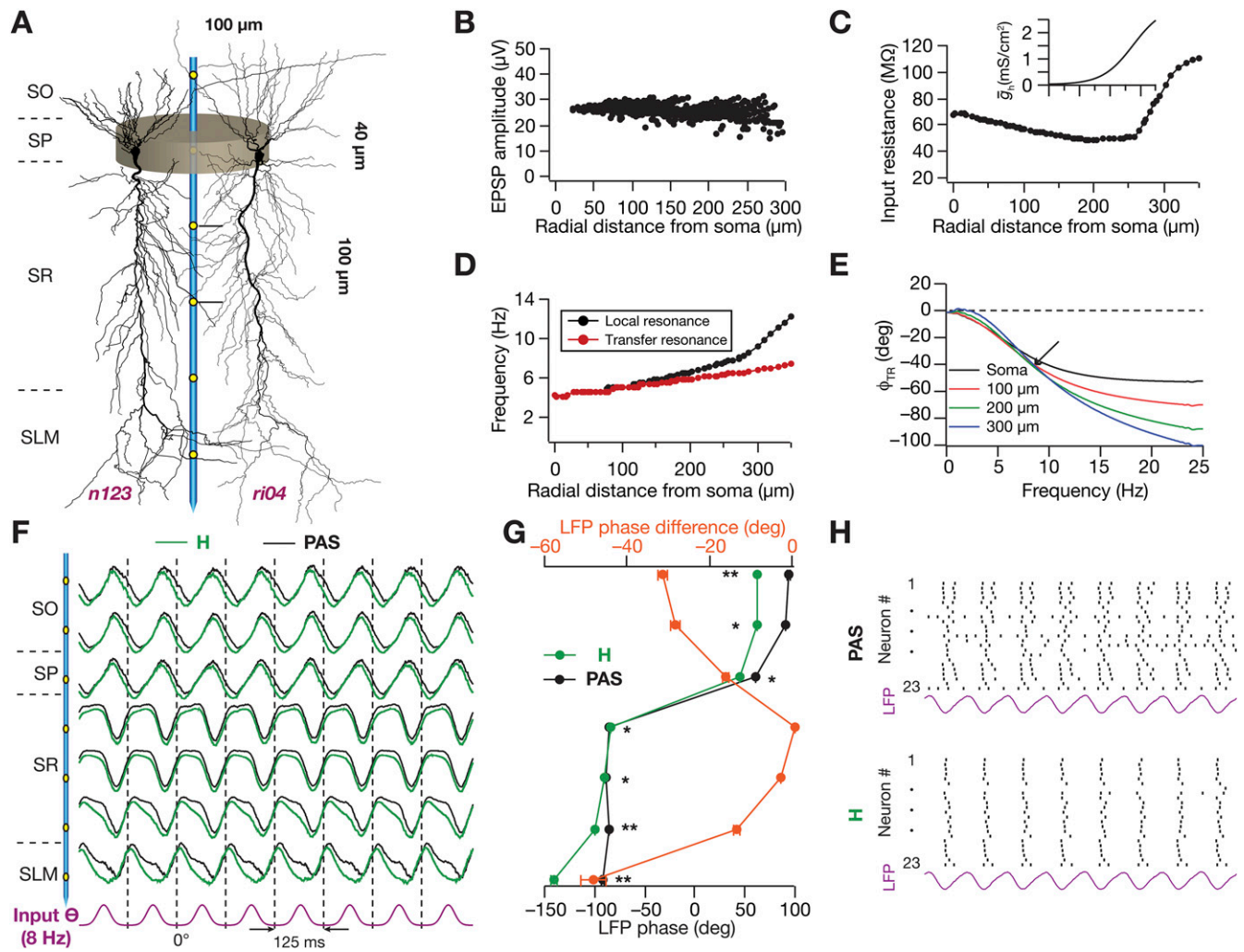


Fig. S3. Model components of the morphological reconstruction *ri04* and computation of LFPs and spike phase from a morphologically heterogeneous neuropil. (A) A single electrode with seven recording sites, located at the center of the cylindrical neuropil, spanned all strata of the CA1. The two morphologies used (*n123* and *ri04*) are depicted. (B–D) Model parameters associated with the morphology *ri04*. (B) Distribution of unitary somatic EPSP amplitudes (V_{UEPSP}) as a function of radial distance from the soma, depicting distance invariance of V_{UEPSP} . (C and D) Input resistance (C) and local and transfer resonance frequency (D) in the presence of a sigmoidal gradient of HCN conductance (C, Inset), all plotted along the somatoapical trunk. (E) Transfer impedance phase profile for four different locations along the somatoapical trunk. Arrow indicates the synchronization frequency at ~ 8 Hz. (F) Normalized LFP traces (1 s) computed from a neuropil with a heterogeneous population of the two morphologies in the presence (H) and the absence (PAS) of HCN channels, plotted with reference to the excitatory input θ . (G, Bottom axis) LFP phase in the presence (H) and the absence (PAS) of HCN channels (mean \pm SEM, 10 cycles) at each recording site, with reference to the excitatory input θ . (G, Top axis) LFP phase difference between the case where HCN channels were present (H) and corresponding passive case (PAS) for each recording site. $*P < 0.05$, $**P < 0.005$ (Wilcoxon signed-rank test). (H) Raster plot of spike timings for 23 neurons and corresponding SP LFP, in the presence (H) and the absence (PAS) of HCN channels.

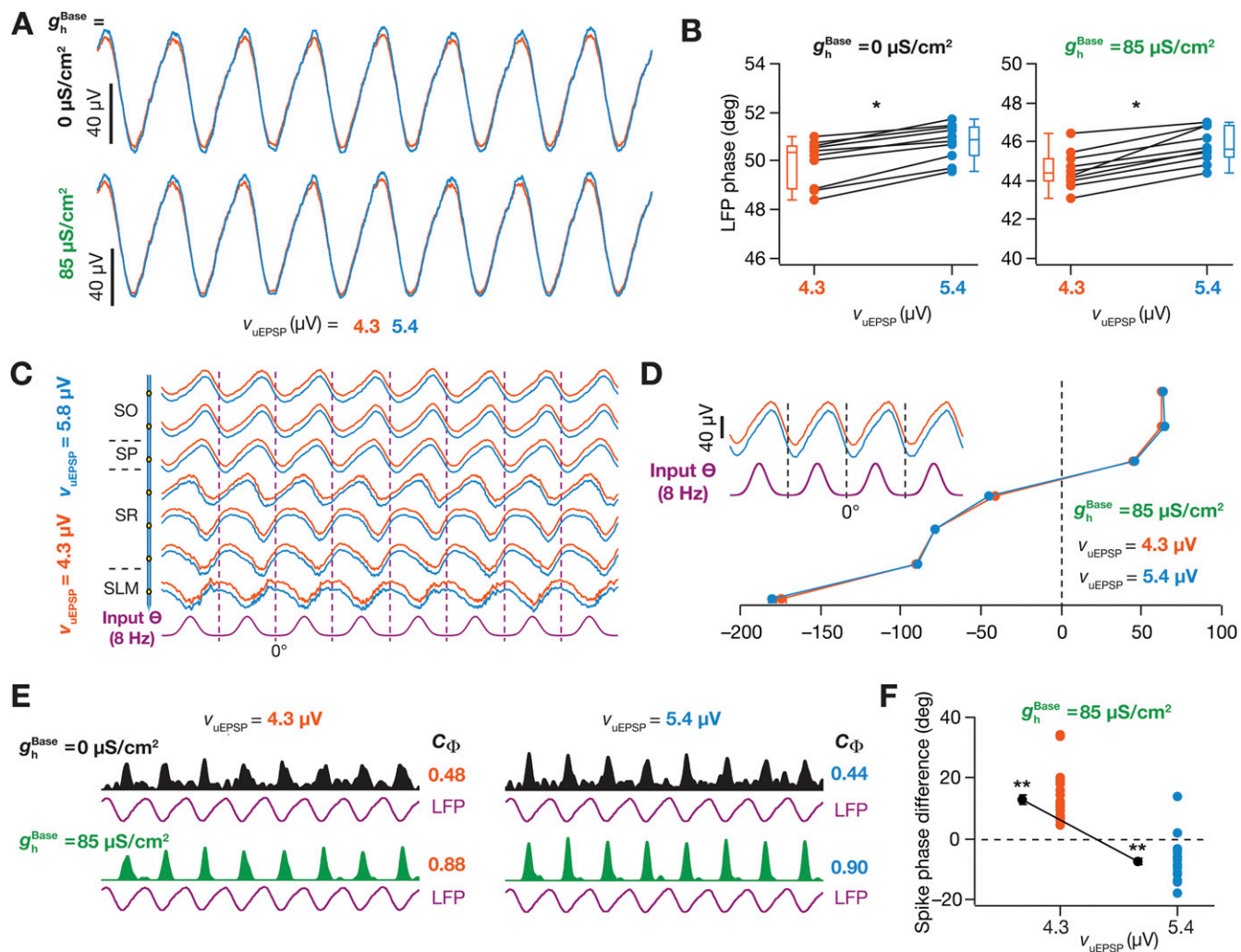


Fig. 54. Regulation of LFPs and spike phase by excitatory synaptic scaling. (A) SP LFP traces (1 s) for two different values of unitary EPSP amplitude (v_{UEPSP}) plotted in the absence ($g_h^{\text{Base}} = 0 \mu\text{S}/\text{cm}^2$) and the presence ($g_h^{\text{Base}} = 85 \mu\text{S}/\text{cm}^2$) of HCN channels. Note that the example traces for the default value of v_{UEPSP} ($4.8 \mu\text{V}$) for $g_h^{\text{Base}} = 0 \mu\text{S}/\text{cm}^2$ and $85 \mu\text{S}/\text{cm}^2$ are shown in Fig. 2A. The chosen range of v_{UEPSP} ensured that there was no depolarization-induced block of spike (high excitability) or failure to reach threshold (low excitability). (B) Quantification of LFP phase across 10 different cycles with reference to the excitatory input θ for corresponding traces shown in A. * $P < 0.05$ (Wilcoxon signed-rank test). (C) Normalized LFP traces (1 s) for different strata for two values of v_{UEPSP} , depicting changes in LFP phase with reference to excitatory input θ for $g_h^{\text{Base}} = 85 \mu\text{S}/\text{cm}^2$. (D) Quantification of the strata-matched LFP phase (10 cycles; mean \pm SEM) with reference to the excitatory input θ for corresponding traces shown in C. (E) Population spike time histograms (1 s) with corresponding SP LFP for two different v_{UEPSP} values, with $g_h^{\text{Base}} = 0 \mu\text{S}/\text{cm}^2$ and $85 \mu\text{S}/\text{cm}^2$. Note that there is no significant difference in spike-phase coherence with change in v_{UEPSP} , either in the presence or in the absence of HCN channels. (F) Spike-phase difference (mean \pm SEM) for each neuron plotted for two different values of v_{UEPSP} with g_h^{Base} fixed at $85 \mu\text{S}/\text{cm}^2$. The cycle-matched phase difference is between spikes obtained with $v_{\text{UEPSP}} = 4.3 \mu\text{V}$ or $5.4 \mu\text{V}$ and spikes obtained with $v_{\text{UEPSP}} = 4.8 \mu\text{V}$ (the baseline value). $n = 22$ for $v_{\text{UEPSP}} = 4.3 \mu\text{V}$ and $n = 24$ for $v_{\text{UEPSP}} = 5.4 \mu\text{V}$. ** $P < 0.005$ (Student's t test on the null hypothesis of no spike-phase difference). Note that here we are comparing the impact of excitatory synaptic scaling on LFP and spike phases and not the impact of HCN channels under different values of v_{UEPSP} (which was reported in Fig. 4A–C). Although the impact of HCN channels on LFP and spike phases was comparable across v_{UEPSP} values (Fig. 4A–C), here we noted that increase in v_{UEPSP} introduced a small, but significant lag in the SP LFP phase (B) and a significant lead in the spike phase (F). Further, unlike the LFP phase lead observed with the introduction of HCN channels (Figs. 2A and B and 4A), the phase shift achieved with synaptic scaling was not consistent across different strata (D) as a result of differential distribution of excitatory and inhibitory synapses. The lead in spike phase achieved with increase in v_{UEPSP} was a direct consequence of the phase lag in SP LFP (B) and the propensity for the membrane voltage to reach threshold earlier with a larger excitatory drive.

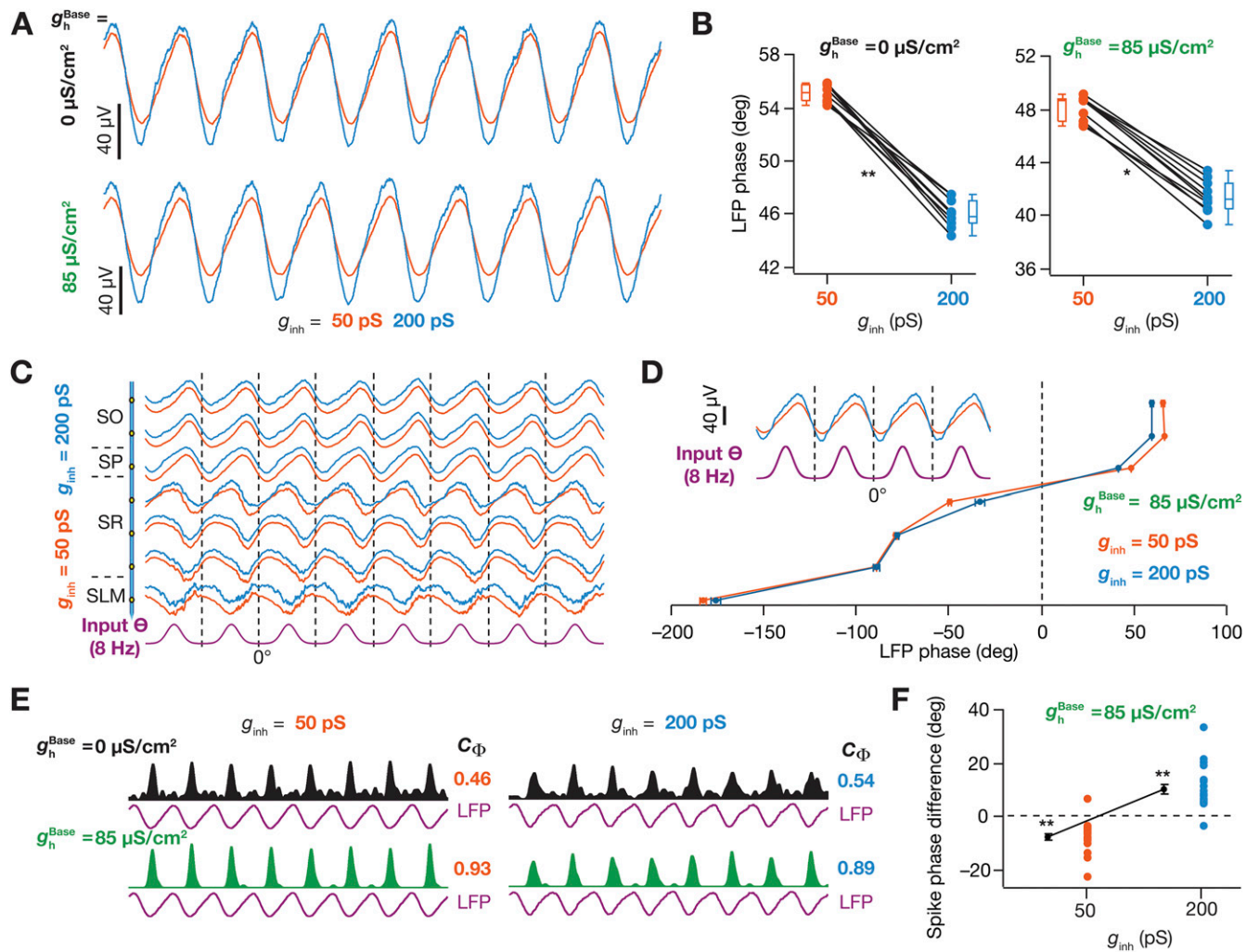


Fig. S5. Regulation of LFPs and spike phase by inhibitory synaptic scaling. (A) SP LFP traces (1 s) for two different values of inhibitory synaptic conductance (g_{inh}) plotted in the absence ($g_h^{Base} = 0 \mu\text{S}/\text{cm}^2$) and the presence ($g_h^{Base} = 85 \mu\text{S}/\text{cm}^2$) of HCN channels. Note that the example traces for the default value of g_{inh} (100 pS) for $g_h^{Base} = 0 \mu\text{S}/\text{cm}^2$ and $85 \mu\text{S}/\text{cm}^2$ are shown in Fig. 2A. (B) Quantification of LFP phase across 10 different cycles with reference to the excitatory input θ for corresponding traces shown in A. $*P < 0.05$, $**P < 0.005$ (Wilcoxon signed-rank test). (C) Normalized LFP traces (1 s) for different strata for two values of g_{inh} , depicting changes in LFP phase with reference to excitatory input θ for $g_h^{Base} = 85 \mu\text{S}/\text{cm}^2$. (D) Quantification of the strata-matched LFP phase (10 cycles; mean \pm SEM) with reference to the excitatory input θ for corresponding traces shown in C. (E) Population spike time histograms (1 s) with corresponding SP LFP for two different g_{inh} values, with $g_h^{Base} = 0 \mu\text{S}/\text{cm}^2$ and $85 \mu\text{S}/\text{cm}^2$. Note that there is no significant difference in spike-phase coherence with change in g_{inh} , either in the presence or in the absence of HCN channels. (F) Spike-phase difference (mean \pm SEM) for each neuron plotted for two different values of g_{inh} , with g_h^{Base} fixed at $85 \mu\text{S}/\text{cm}^2$. The cycle-matched phase difference is between spikes obtained with $g_{inh} = 50$ pS or 200 pS and spikes obtained with $g_{inh} = 100$ pS (the baseline value). $n = 24$ for $g_{inh} = 50$ pS and $n = 23$ for $g_{inh} = 200$ pS. $**P < 0.005$ (Student's t test on the null hypothesis of no spike-phase difference). Note that here we are comparing the impact of inhibitory synaptic scaling on LFP and spike phases and not the impact of HCN channels under different values of g_{inh} (which was reported in Fig. 4D–F). Although the impact of HCN channels on LFP and spike phases was comparable across g_{inh} values (Fig. 4D–F), here we noted that increase in g_{inh} introduced a significant lead in the SP LFP phase (B) and a significant lag in the spike phase (F). Further, unlike the LFP phase lead observed with the introduction of HCN channels (Figs. 2A and B and 4D), the phase shift achieved with synaptic scaling was not consistent across different strata (D) as a result of differential distribution of excitatory and inhibitory synapses. The lag in spike phase achieved with increase in g_{inh} was a direct consequence of the phase lead in SP LFP (B) and the propensity for the membrane voltage to reach threshold later with a larger inhibitory drive.

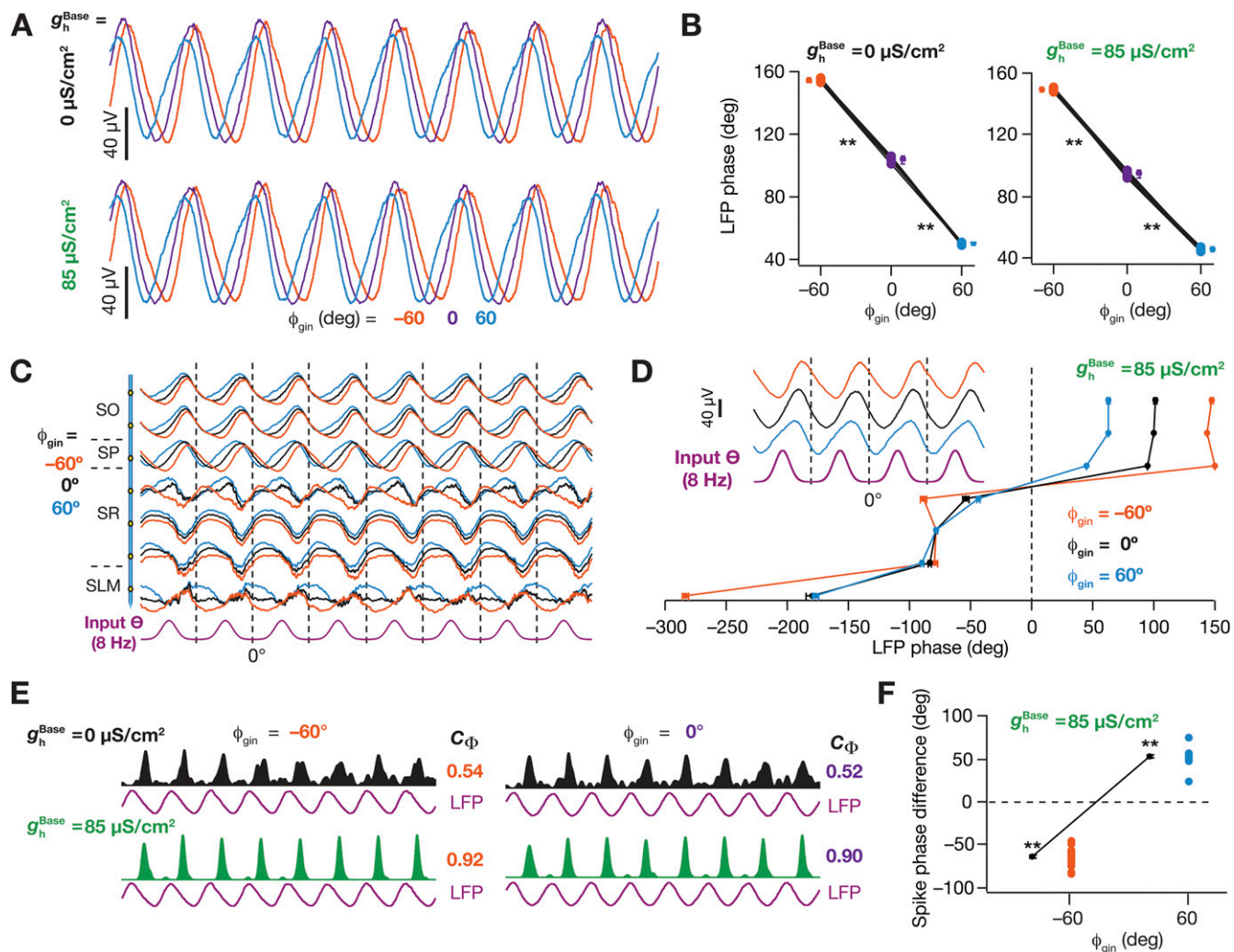


Fig. S6. Critical regulation of LFPs and spike phase by the phase difference between the excitatory and inhibitory theta inputs. (A) SP LFP traces (1 s) for three different values of the phase difference between the excitatory and inhibitory theta inputs (ϕ_{gin}) plotted in the absence ($g_h^{Base} = 0 \mu\text{S}/\text{cm}^2$) and the presence ($g_h^{Base} = 85 \mu\text{S}/\text{cm}^2$) of HCN channels. Note that the example traces for the default value of ϕ_{gin} (60°) for $g_h^{Base} = 0 \mu\text{S}/\text{cm}^2$ and $85 \mu\text{S}/\text{cm}^2$ are also shown in Fig. 2A. (B) Quantification of LFP phase across 10 different cycles with reference to the excitatory input θ for corresponding traces shown in A. $**P < 0.005$ (Wilcoxon signed-rank test). (C) Normalized LFP traces (1 s) for different strata for three values of ϕ_{gin} , depicting changes in LFP phase with reference to excitatory input θ for $g_h^{Base} = 85 \mu\text{S}/\text{cm}^2$. (D) Quantification of the strata-matched LFP phase (10 cycles; mean \pm SEM) with reference to the excitatory input θ for corresponding traces shown in C. (E) Population spike time histograms (1 s) with corresponding SP LFP for three different ϕ_{gin} values, with $g_h^{Base} = 0 \mu\text{S}/\text{cm}^2$ and $85 \mu\text{S}/\text{cm}^2$. Note that there is no significant difference in spike-phase coherence with change in ϕ_{gin} , either in the presence or in the absence of HCN channels. (F) Spike-phase difference (mean \pm SEM) for each neuron plotted for three different values of ϕ_{gin} , with g_h^{Base} fixed at $85 \mu\text{S}/\text{cm}^2$. The cycle-matched phase difference ($n = 24$) is between spikes obtained with $\phi_{gin} = -60^\circ$ or 60° and spikes obtained with $\phi_{gin} = 0^\circ$. $**P < 0.005$ (Student's t test on the null hypothesis of no spike-phase difference). Note that here we are comparing the impact of excitatory–inhibitory phase difference on LFP and spike phases and not the impact of HCN channels under different values of ϕ_{gin} (which was reported in Fig. 4 G–I). Although the impact of HCN channels on LFP and spike phases was comparable across ϕ_{gin} values (Fig. 4 G–I), here we noted that increase in ϕ_{gin} introduced a significant lead in the SP LFP phase (B) and a significant lag in the spike phase (F). Further, unlike the LFP phase lead observed with the introduction of HCN channels (Figs. 2 A and B and 4G), when compared across strata, changes in ϕ_{gin} resulted in a huge phase change only in the SO and SP layers, but not in the SR (F), because inhibitory synapses impinged on perisomatic compartments. The lag in spike phase achieved with increase in ϕ_{gin} was a direct consequence of the phase lead in SP LFP (B).

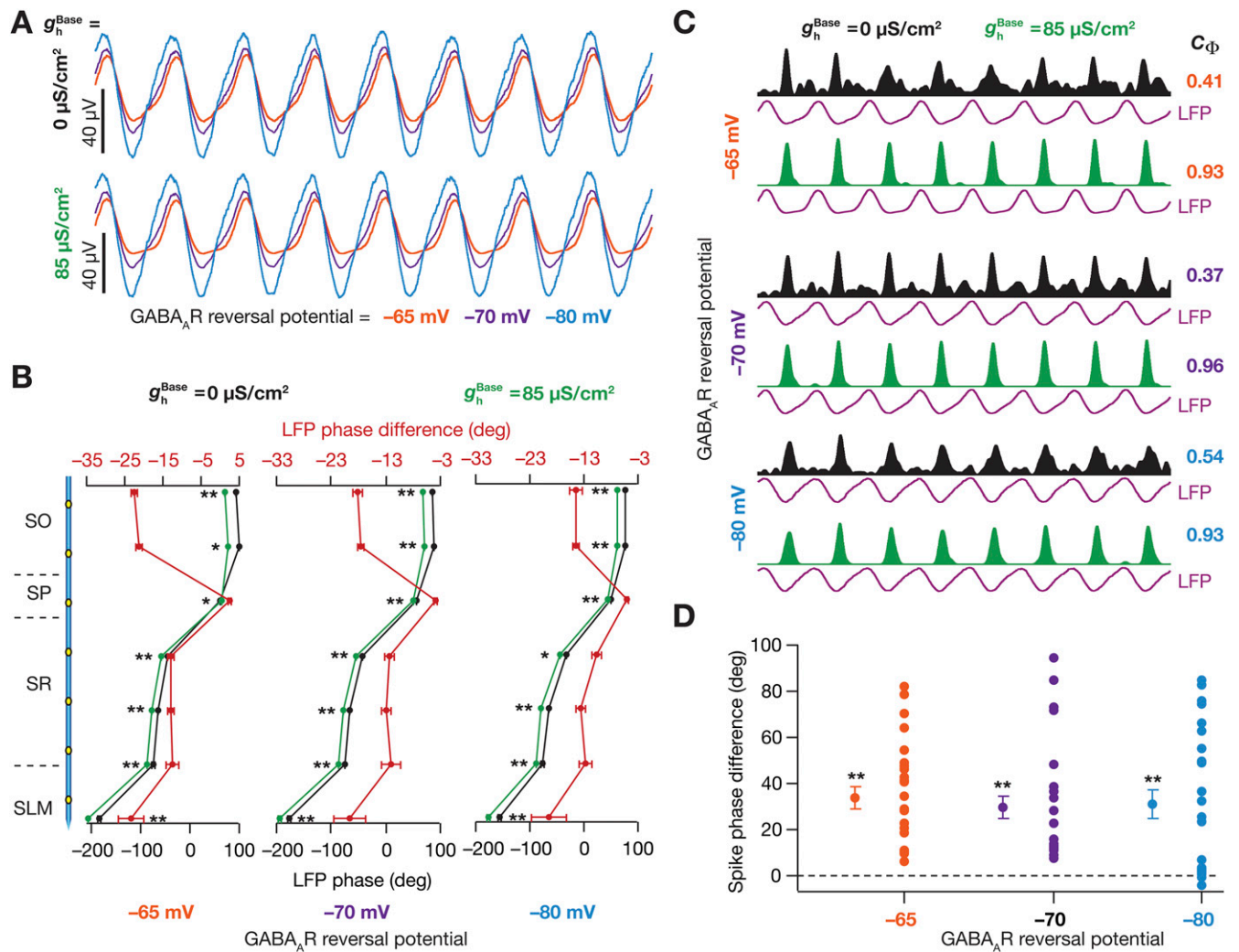


Fig. S7. Regulation of LFP and spike phases by HCN channels was invariant to changes in the reversal potential of GABA_A receptors. (A) SP LFP traces for the passive case (PAS) and in the presence of HCN channels (H) for three different values of GABA_AR reversal potential. (B, Bottom axis) LFP phase with reference to the excitatory input θ (mean \pm SEM, 10 cycles), computed in the presence ($g_h^{\text{Base}} = 85 \mu\text{S}/\text{cm}^2$) and the absence ($g_h^{\text{Base}} = 0 \mu\text{S}/\text{cm}^2$) of HCN channels for three different values of GABA_AR reversal potential. (B, Top axis) Strata-matched phase difference between LFPs obtained with $g_h^{\text{Base}} = 85 \mu\text{S}/\text{cm}^2$ and $0 \mu\text{S}/\text{cm}^2$, computed for three different values of GABA_AR reversal potential. * $P < 0.05$, ** $P < 0.005$ (Wilcoxon signed-rank test). (C) Population spike time histograms (1 s) with corresponding SP LFP for three different GABA_AR reversal potential values, with $g_h^{\text{Base}} = 0 \mu\text{S}/\text{cm}^2$ and $85 \mu\text{S}/\text{cm}^2$. (D) Cycle-matched difference between spike phases obtained with $g_h^{\text{Base}} = 85 \mu\text{S}/\text{cm}^2$ and with $g_h^{\text{Base}} = 0 \mu\text{S}/\text{cm}^2$ for different neurons (mean \pm SEM), plotted for each value of GABA_AR reversal potential ($n = 24$ neurons for GABA_AR reversal potential = -80 mV). ** $P < 0.005$ (Student's t test on the null hypothesis of no spike-phase difference).

